

Structure- and fluid-borne acoustic power sources induced by turbulent flow in 90° piping elbows

S.A. Hambric*, D.A. Boger, J.B. Fahline, R.L. Campbell

The Pennsylvania State University, Applied Research Laboratory, PO Box 30, State College, PA 16804, USA

Received 12 May 2008; accepted 6 October 2009

Available online 16 December 2009

Abstract

The structure- and fluid-borne vibro-acoustic power spectra induced by turbulent fluid flow over the walls of a continuous 90° piping elbow are computed. Although the actual power input to the piping by the wall pressure fluctuations is distributed throughout the elbow, equivalent total power inputs to various structural wavetypes (bending, torsion, axial) and fluid (plane-waves) at the inlet and discharge of the elbow are computed. The powers at the elbow “ports” are suitable inputs to wave- and statistically-based models of larger piping systems that include the elbow. Calculations for several flow and structural parameters, including pipe wall thickness, flow speed, and flow Reynolds number are shown. The power spectra are scaled on flow and structural–acoustic parameters so that levels for conditions other than those considered in the paper may be estimated, subject to geometric similarity constraints (elbow radius/pipe diameter). The approach for computing the powers (called CHAMP – combined hydroacoustic modeling programs), which links computational fluid dynamics, finite element and boundary element modeling, and efficient random analysis techniques, is general, and may be applied to other piping system components excited by turbulent fluid flow, such as U-bends and T-sections.

© 2009 Elsevier Ltd. All rights reserved.

Keywords: Structural–acoustics; Fluid dynamics; Structure-borne sound; Acoustic power; Elbow; Piping; Turbulent boundary layer; Finite element; Boundary element; Computational fluid dynamics; Scaling

1. Introduction

Noise sources due to turbulent fluid flow through piping elbows are difficult to quantify. As the fluid flows through an elbow, strong pressure gradients develop, which generate secondary flow fields through and downstream of the elbow, such as those shown in Fig. 1. Wall pressure fluctuations beneath turbulent pipe boundary layer flow excite the piping walls, which then vibrate and radiate sound into the internal (and external) acoustic fluid. The wall pressures therefore cause structure-borne and fluid-borne sound waves to emanate from the inlet and outlet of the elbow. Several researchers have investigated the fluid-dynamic and structural–acoustic behavior of fluid-filled piping systems, see for example, the review articles by Wiggert and Tijsseling (2001) and Hambric et al. (2002). Papers which focus specifically on elbow excitation and response are less common, and tend to examine the structural–acoustic or fluid-dynamic

*Corresponding author.

E-mail address: sah19@arl.psu.edu (S.A. Hambric).

Nomenclature			
A	cross-sectional area of the fluid or structure	P_1, P_2	empirical power formulae coefficients
a	mean radius of pipe wall	R	correlation function
B, b	physical and modal damping matrices	Re_D	Reynolds number, $U_o D/\nu$
$C(\omega), \mathbf{c}(\omega)$	physical and modal attached structure matrices	t	time
c_B, c_s, c_o	bending, shear, and acoustic sound speeds	u	local velocity
D	pipe diameter	$U_o, U_c, U_{\text{edge}}$	bulk, convective, and edge flow velocities
E	Young's modulus	v	structural vibration (velocity)
$E[\]$	expected value	w	displacement
f	circular frequency (Hz)	\bar{x}, \bar{x}'	response and excitation locations
F_1	Menter blending function	y	distance from pipe wall
$F(\omega)$	applied force vector	y^+	dimensionless distance from pipe wall
G	shear modulus	Z	impedance
G_{pp}, G_{vv}	wall pressure and pipe vibration CSDs	z	axial direction
$\mathbf{G}_{FF}(\omega), \mathbf{G}_{ff}(\omega)$	physical and modal force CSD matrices	$\mathbf{Z}(\omega), \mathbf{z}(\omega)$	physical and modal impedance matrices
G_{power}	power in various wavetypes	α_1, α_3	TBL decay coefficients
$\mathbf{G}_{\psi\psi}(\omega)$	modal amplitude cross-spectral density matrix	Γ	normalized TBL cross-spectral density function
$\mathbf{H}(\omega), \mathbf{h}(\omega)$	physical and modal frequency response functions	δ	boundary layer thickness
h_i	impulse response function	δ^*	boundary layer displacement thickness
H	frequency response function	Δ_1, Δ_3	separation distances in streamwise and cross-flow directions
J_1	Bessel function of the first kind	ε	turbulence dissipation rate
J	polar moment of inertia	θ	circumferential angle
k	wavenumber	μ	dynamic viscosity
\bar{k}	turbulence kinetic energy	ν	kinematic viscosity
k_c, k_B, k_p, k_z	convective, bending, cutoff, and axial wavenumbers	ξ	separation vector between loaded points
K, k	physical and modal stiffness matrices	ρ	cross-covariance
L	elbow length (with sections of upstream and downstream piping)	ρ_s, ρ_o	structural and fluid density
ℓ	turbulence length scale	$\sigma_{\omega 2}$	Prandtl number (closure coefficient)
M, m	physical and modal mass matrices	τ	time delay
n	circumferential harmonic	$\phi_{pp}(\omega)$	wall pressure autospectrum
p	wall pressure	$\Phi_{pp}(\xi, \omega)$	wall pressure cross-spectral density (CSD)
		ϕ_m	mode shape
		Φ	matrix of mode shapes
		$\psi(\omega)$	vector of modal amplitudes
		ω	radial frequency (rad/s)
		$\bar{\omega}$	dissipation per unit turbulent kinetic energy

mechanisms individually. This paper, therefore, describes the coupled fluid-dynamic and structural–acoustic behavior of flow-excited elbows.

Piping wall motion in the radial, longitudinal, or torsional directions is typically characterized using its circumferential harmonic components, where for example,

$$w(\theta, z, t) = \left(\sum_{n=1}^{\infty} W_n \cos(n\theta) + \sum_{n=1}^{\infty} V_n \sin(n\theta) \right) e^{-ik_z z + i\omega t},$$

where $w(\theta, z, t)$ is the pipe wall motion as a function of axial location z and angular location θ , W_n , and V_n are coefficients for each harmonic n , k_z is the axial wavenumber, and ω is the radial frequency. When $n = 0$, the pipe cross-section “breathes”, with no phase variation about its circumference (the sin term goes to zero and the cos term is constant at 1 for all θ). For flexural motion when $n = 1$, the entire cross-section moves transversely, and the pipe effectively acts as a beam in flexure. For flexural motion where $n > 1$, the pipe wall deforms, and the so-called “lobar” modes occur. Within the pipe, acoustic pressure fluctuations in the fluid propagate as planar waves below the cut-on frequency of modes across the fluid cross-section. In this article, only plane acoustic waves are considered.

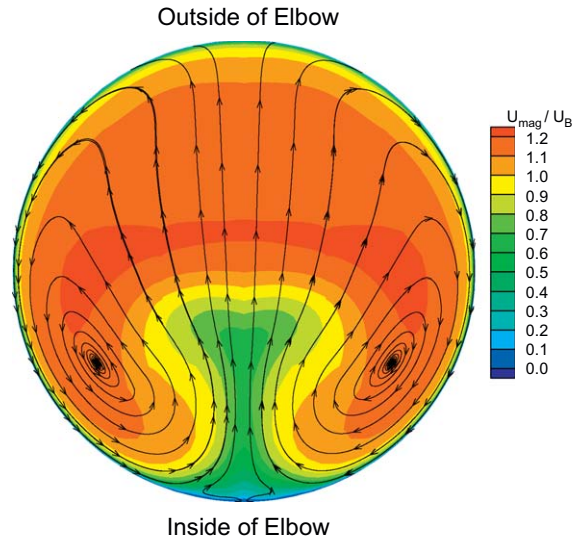


Fig. 1. Secondary flow pattern at outlet of pipe elbow; contour is of total local velocity normalized to bulk velocity. Bottom of plot is at the inside of the bend.

Everstine (1986) derived a low-frequency finite element modeling technique that simulates plane acoustic wave propagation in the working fluid and bending ($n = 1$) and longitudinal waves in the piping. The formulation was validated against measurements of structural–acoustic transfer functions of an oil-filled copper pipe with an elbow made by Davidson and Smith (1969, 1972). Higher frequency structural–acoustic modeling of pipes with elbows has been discussed by Manning (2002), who used statistical energy analysis (SEA) to investigate the transfer of energy between piping wall modes and acoustic fluid modes.

Transfer matrix techniques, where sections of piping and other components (pumps and valves, for example) are modeled using matrices of transmission and reflection coefficients, have been investigated by several authors. Lesmez et al. (1990) and Hwang (2002), among others, have used impedance matrices to relate fluctuating forces (or pressures) and velocities at discrete frequencies. Coupling between all structural and acoustic wavenumbers may be included in the matrices. Other authors, such as Stokes et al. (2001), use wave transmission line (WTL) approaches, where the matrices relate wave amplitudes (instead of impedances) of structural and acoustic wavenumbers. In either case, full coupling between all wavenumbers may be included in the analysis. For example, bending waves incident on an elbow could transmit compressional waves into the outlet of the elbow. The advantage to using transfer matrix techniques is that once assembled, the models are easy to solve. However, the scattering matrices for each of the components in the modeled system must be generated prior to using the technique. Analytic techniques, finite element models, or measurements may all be used to generate the matrices. For example, Conti et al. (2001) measured scattering matrices (suitable for use in the WTL approach) of a fluid-filled elbow.

Various experimental and numerical studies have been made of the turbulent flow within elbows. Enayet et al. (1982) measured the steady and unsteady flow within and downstream of an elbow with a radius of curvature to diameter ratio (R/D) of 2.8 at a Reynolds number (based on bulk velocity and pipe diameter) of 43 000. Kawamura and Takahashi (1996) measured similar quantities for a much tighter elbow ($R/D = 0.55$) and at higher Reynolds numbers (up to 1 000 000). Comparing the data between the two studies, the tighter radius elbow generated significantly higher downstream turbulence intensities. In both cases, the secondary flow and turbulence generated by the elbows decayed as the flow traveled away from the elbow, eventually returning to fully developed straight pipe flow.

Anwer and So (1993) measured the behavior of flow through a U-bend (a 180° elbow) with an R/D of about 6. Later, Boersma and Nieuwstadt (1996) performed numerical large eddy simulation (LES) studies on a similar bend. Both authors discuss the formation of various cells in the secondary flow patterns, such as the ones shown in Fig. 1. The flow speed is quite low near the inside radius of the bend, and increases toward the center. The flow and pressure gradients cause the formation of vortices in the flow, as well as increased turbulence levels.

Although the individual behavior of the flow fields and structural–acoustic transmission mechanisms of fluid-filled pipes has been studied, insufficient work has been done on modeling the coupling of the fluctuating forces in the fluid flow to the structural–acoustic response of the elbow, surrounding piping, and internal fluid. In this paper, the

structural–acoustic response of an elbow due to internal turbulent flow is investigated. The analysis approach is based on random structural–acoustic analysis procedures developed and applied previously in the aerospace (Powell, 1958; Wilby, 1967; Jacobs et al., 1970), and nuclear (Au-Yang and Connelly, 1977) industries, and later improved and formalized into the CHAMP (Combined HydroAcoustic Modeling Programs) procedure at ARL/Penn State (Hambric et al., 2004, 2005). Computational fluid dynamics (CFD) analyses are used along with empirical formulas to estimate wall pressure cross-spectra which are applied to finite element (FE) and boundary element (BE) models of the piping and internal working fluid. The resulting structure- and fluid-borne power levels at the inlet and outlet of the elbow are computed, along with their circumferential harmonic components. These power levels are effectively equivalent source terms at the “ports” of the elbow, suitable for use in transfer matrix or SEA models.

Several conditions are considered, including variable pipe wall thickness, flow speed, and flow Reynolds number. Scaling relationships are then derived to collapse the power spectra for each wavetype generated for each condition. Empirical curve fits to the collapsed data are presented, which may be used by future investigators to estimate source levels for geometrically similar pipes with different dimensions, materials, and flow conditions.

2. Problem definition and assumptions

Fig. 2 shows a straight inlet pipe, a 90° elbow with bend radius/nominal diameter ratio of 1.5 (typical of off the shelf piping elbows), and a long straight discharge pipe. The flow entering the elbow region is assumed to be fully developed turbulent pipe flow, with a Reynolds number (based on diameter) of at least 4000, so that no laminar or transition regions exist anywhere in the pipe. The steady flow rate is assumed to be constant, and all unsteady Reynolds stresses within the flow and resulting wall pressure fluctuations are assumed to be stationary and ergodic processes.

The structure is assumed to be continuous, with no structural impedance discontinuities at any joints or end conditions. This assumption essentially dictates smooth, continuous, homogeneous physical and material properties throughout the elbow. In the future, discontinuities such as flanges may be considered. These sorts of discontinuities lead to structural–acoustic acceptance functions for a wavenumber range of the turbulent wall pressure fluctuations not considered in this study.

We also assume an important relationship between the flow speed and structural wavespeeds. Namely, the ratio of fluid to structural wavespeeds is assumed to be small, such that the wavenumber ratio $k/k_c < 0.1$ (where k_c is the convective wavenumber of the flow, ω/U_c , where ω is radial frequency, and U_c is convective velocity). This assumption allows us to use a computationally efficient cross-spectral density model (described in Section 3.2.2) to simulate the spatial coherence of the pressure fluctuations. This assumption is valid for many practical conditions, particularly for heavy, slow moving working fluids.

We analyze several combinations of flow and structural parameters so that scaling of the power injected into various wavytypes may be attempted. CFD analyses at Re_D of 2×10^6 and 20×10^6 were performed. The data from the analyses may be scaled to different pipe sizes, flow speeds, and fluid properties. We set the fluid properties to those of water for

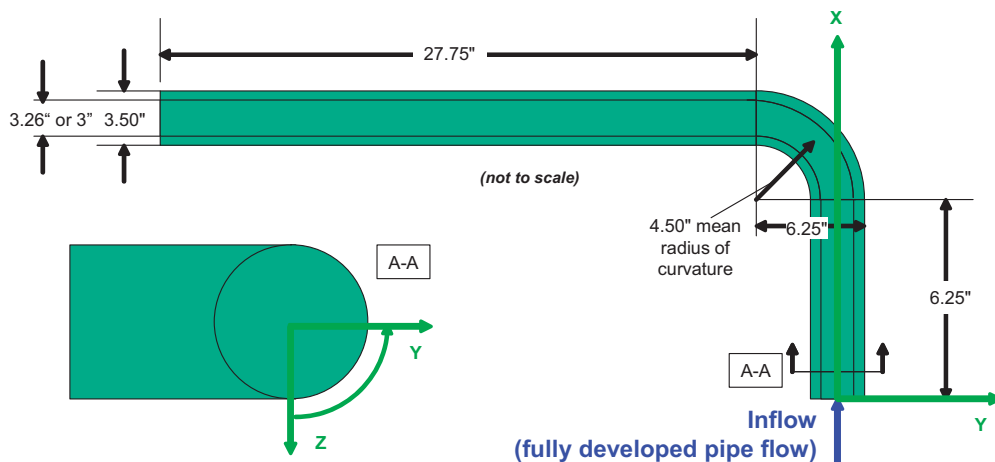


Fig. 2. TBL excited piping system with 90° elbow, inlet at lower right, discharge at upper left.

all studies presented here, and consider flow speeds ranging from 21 to 105 m/s. Finally, two pipe sizes are analyzed: Schedules 10 and 40 steel 76.2 mm (3 in) pipe.

3. Procedure for estimating power source levels

3.1. Champ approach

Fig. 3 shows a schematic of a pipe section excited by turbulent boundary layer (TBL) flow, which varies significantly over the body. Following the definitions of Strawderman (1969), the vibration response at any point on a structure is found by integrating over the loaded region:

$$v_i(\bar{x}, t) = \int_{\Delta_1} \int_{\Delta_3} \int_{\tau} p(\Delta_1, \Delta_3, t - \tau) h_i(\bar{x}, \bar{x}', \tau) d\Delta_1 d\Delta_3 d\tau, \quad (1)$$

where $v_i(\bar{x}, t)$ is a velocity response in direction i at time t , \bar{x} is a vector in space defining the response location, and τ is the time delay between t and a future time t' . The loaded region is represented by a surface parameterized by coordinates Δ_1 and Δ_3 . The impulse response function $h_i(\bar{x}, \bar{x}', t, t') = v_i(\bar{x}, t)$ when $p(\Delta_1, \Delta_3, t) = \delta(\bar{x} - \bar{x}')\delta(t - t')$, where δ denotes the Dirac delta function and \bar{x}' is a vector in space defining the location at parametric coordinates (Δ_1, Δ_3) . Note that the response location \bar{x} need not lie within the forced region. For example, the response location might be at a downstream section of pipe, or at a pipe support.

Usually it is acceptable to assume that $v_i(\bar{x}, t)$ has a negligible effect on $p(\Delta_1, \Delta_3, t - \tau)$, so that $p(\Delta_1, \Delta_3, t - \tau)$ is estimated assuming “blocked” boundary conditions, e.g., the fluid flows over a rigid surface. When this assumption is made, $p(\Delta_1, \Delta_3, t - \tau)$ may be computed using CFD analysis of flow over a stationary grid of points, and $h_i(\bar{x}, \bar{x}', \tau)$ may be computed using numerical techniques like finite elements and boundary elements.

For uncoupled, “blocked” response, the cross-correlation of the vibration response between points \bar{x}_1 and \bar{x}_2 and times t_1 and t_2 is defined as

$$R_{vv}(\bar{x}_1, \bar{x}_2, t_1, t_2) = \int_{\bar{x}'_1} \int_{\bar{x}'_2} \int_{\tau_1} \int_{\tau_2} E[p(\bar{x}'_1, t_1 - \tau_1)p(\bar{x}'_2, t_2 - \tau_2)] h(\bar{x}_1, \bar{x}'_1, \tau_1) h(\bar{x}_2, \bar{x}'_2, \tau_2) d\bar{x}'_1 d\bar{x}'_2 d\tau_1 d\tau_2, \quad (2)$$

where $E[]$ denotes the expected value. The expected value of the pressures in Eq. (2) is the cross-correlation of the pressure field, so that the cross-correlation of the vibration response may be re-written as

$$R_{vv}(\bar{x}_1, \bar{x}_2, t_1, t_2) = \int_{\bar{x}'_1} \int_{\bar{x}'_2} \int_{\tau_1} \int_{\tau_2} R_{pp}(\bar{x}'_1, \bar{x}'_2, t_1 - \tau_1, t_2 - \tau_2) h(\bar{x}_1, \bar{x}'_1, \tau_1) h(\bar{x}_2, \bar{x}'_2, \tau_2) d\bar{x}'_1 d\bar{x}'_2 d\tau_1 d\tau_2. \quad (3)$$

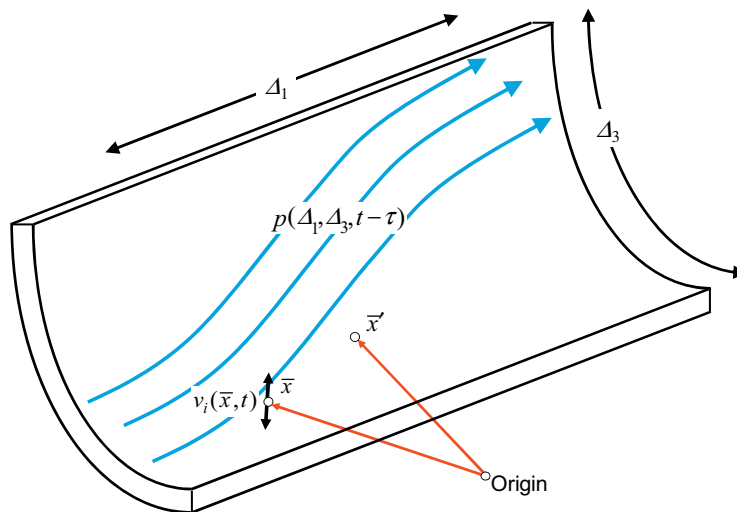


Fig. 3. Schematic of pipe section excited by TBL flow.

Assuming the pressure cross-correlation is statistically stationary over time, Eq. (3) may be transformed from time to frequency, and the cross-power spectral density (CSD) of velocity is defined as

$$G_{vv}(\bar{x}_1, \bar{x}_2, \omega) = \int_{\bar{x}'_1} \int_{\bar{x}'_2} H^*(\bar{x}_1, \bar{x}'_1, \omega) G_{pp}(\bar{x}'_1, \bar{x}'_2, \omega) H(\bar{x}_2, \bar{x}'_2, \omega) d\bar{x}'_1 d\bar{x}'_2, \quad (4)$$

where $H(\bar{x}_1, \bar{x}'_1, \omega) = \int_{-\infty}^{\infty} h(\bar{x}_1, \bar{x}'_1, t) e^{i\omega t} dt$ corresponds to the velocity response at point \bar{x}_1 due to a sinusoidal excitation at frequency ω at point \bar{x}'_1 , commonly denoted a frequency response function (FRF). FRF functions may be generated from analytic or numerical (FE/BE) models, and from measurements. $G_{pp}(\bar{x}'_1, \bar{x}'_2, \omega)$ is the one-sided cross-spectral density of pressure, defined by

$$G_{pp}(\bar{x}'_1, \bar{x}'_2, \omega) = \frac{1}{\pi} \int_{-\infty}^{\infty} R_{pp}(\bar{x}'_1, \bar{x}'_2, \tau) e^{i\omega\tau} d\tau. \quad (5)$$

Note that we assume a statistically stationary, ergodic flow field, but not a homogenous one. When calculations are performed for cyclic frequencies f ,

$$G_{pp}(f) = 2\pi G_{pp}(\omega). \quad (6)$$

In practice, the integrations over space in Eq. (4) are replaced with discretized summations, such that

$$G_{vv}(\bar{x}_1, \bar{x}_2, \omega) = \sum_{k=1}^N \sum_{l=1}^N H^*(\bar{x}_1, \bar{x}'_1, \omega) G_{pp}(\bar{x}'_1, \bar{x}'_2, \omega) H(\bar{x}_2, \bar{x}'_2, \omega). \quad (7)$$

These summations are described in detail as multiple input multiple output (MIMO) problems by Bendat and Piersol (2000).

3.1.1. Modal forcing and response

In CHAMP, the CSDs of vibration are computed using modal, rather than physical FRFs. Assuming a time-harmonic dependence of $e^{i\omega t}$, the modal velocity frequency response function matrix $\mathbf{h}(\omega)$ is defined as

$$\mathbf{h}(\omega) = i\omega [-\omega^2 \mathbf{m} + i\omega \mathbf{b} + \mathbf{k} + \mathbf{z}(\omega) + \mathbf{c}(\omega)]^{-1}, \quad (8)$$

where ω is the analysis frequency, \mathbf{k} , \mathbf{b} , \mathbf{m} , $\mathbf{z}(\omega)$, and $\mathbf{c}(\omega)$ are the modal stiffness, damping, mass, fluid-loading, and attached impedance matrices, defined as $\boldsymbol{\phi}^T \mathbf{M} \boldsymbol{\phi}$, $\boldsymbol{\phi}^T \mathbf{B} \boldsymbol{\phi}$, $\boldsymbol{\phi}^T \mathbf{K} \boldsymbol{\phi}$, $\boldsymbol{\phi}^T \mathbf{Z}(\omega) \boldsymbol{\phi}$, and $\boldsymbol{\phi}^T \mathbf{C}(\omega) \boldsymbol{\phi}$ where $\boldsymbol{\phi}$ is a matrix of the structural mode shapes ϕ_m in the absence of fluid-loading effects and \mathbf{M} , \mathbf{B} , \mathbf{K} , $\mathbf{Z}(\omega)$, and $\mathbf{C}(\omega)$ are the mass, damping, stiffness, fluid-loading, and attached impedance matrices in physical coordinates. \mathbf{K} and \mathbf{k} include structural damping effects, and are therefore complex. The mode shapes are assumed to be normalized by the square root of the modal, or generalized masses, such that \mathbf{m} is the identity matrix and the diagonal values of \mathbf{k} correspond to the eigenvalues ω_m^2 . Therefore, the terms in the modal FRF matrix $\mathbf{h}(\omega)$ have the units (velocity)(mass)/(force).

3.1.2. Structural and acoustic coupling matrices

$\mathbf{C}(\omega)$ is a complex matrix containing the stiffness, damping, and mass of any surrounding structural–acoustic systems attached to points on the main, or master structure(s). For example, a numerical tool could be used to generate mode shapes and modal matrices of a pipe elbow, used to populate the \mathbf{m} , \mathbf{b} , \mathbf{k} , and $\boldsymbol{\phi}$ matrices, while an analytic tool could generate impedances of a semi-infinite pipe connected to the ends of the elbow. The semi-infinite pipe impedances would be included in $\mathbf{C}(\omega)$, and converted into modal impedances in $\mathbf{c}(\omega)$.

The fluid loading matrices $\mathbf{Z}(\omega)$ and $\mathbf{z}(\omega)$ are generated using Koopmann and Fahline's lumped parameter BE approach (Koopmann and Fahline, 1996; Koopmann and Fahline, 1997, 2009), and include mass loading (reactive) and damping (resistive, related to sound power radiation) terms. A summary of the unique characteristics of our formulation follows. First, the acoustic equations are written in terms of the elemental variables volume velocity and average pressure. This forces the solution to converge as a function of acoustic element mesh density. Second, the so-called “tripole sources” are used to eliminate nonuniqueness difficulties, following the ideas of Hwang and Chang (1991). Also, thin plate-like elements that deform only in bending are represented acoustically using dipole sources in the same manner as in the papers by Martinez (1990) and Wu (1995). Fourth, great care has been taken to ensure that

the singular fields are integrated correctly over the boundary surface. To do this, we make extensive use of the semi-analytical integration scheme originally described by Engbloom and Nelson (1975) and developed further by a number of researchers (Duong, 1980; Hayami and Brebbia, 1987; Hayami and Matsumoto, 1994; Sgard et al., 1994). Fifth, we construct the acoustic element mesh by grouping structural elements together into larger acoustic elements. This allows us to adjust the structural and acoustic meshes to properly resolve both the structural and acoustic waves without overly refining the acoustic mesh. Finally, because modal coupling matrices are slowly varying functions of frequency, they are interpolated from matrices calculated at sparse intervals over the frequency band of interest (Fahnline, 2000). This speeds up the computations immensely because the coupling matrix can be interpolated much faster than it can be directly calculated.

The fluid loading matrix $\mathbf{Z}(\omega)$ is partitioned into wetted regions surrounding individual components, and each partition is computed separately using block solvers. To couple individual structures via fluid-loading, the mode shapes of the structures would be specified at locations corresponding to the boundary element representation. Eq. (8) therefore allows for structural and fluid coupling of multiple structures.

3.1.3. Velocity response

To compute velocities $V(\omega)$ due to a deterministic applied force vector $F(\omega)$,

$$V(\omega) = \mathbf{H}_{rp}(\omega)F(\omega) = [\boldsymbol{\phi}_{rp}\mathbf{h}(\omega)\boldsymbol{\phi}_{fp}^T]F(\omega) = \boldsymbol{\phi}_{rp}[\mathbf{h}(\omega)f(\omega)] = \boldsymbol{\phi}_{rp}\psi(\omega), \quad (9)$$

where $\mathbf{H}_{rp}(\omega)$ (equal to $[\boldsymbol{\phi}_{rp}\mathbf{h}(\omega)\boldsymbol{\phi}_{fp}^T]$) is the frequency response function matrix (in physical coordinates, with entries equal to velocity/force) with entries at response points “ rp ”, $\boldsymbol{\phi}_{rp}$ are the mode shapes at the response points “ rp ”, $\boldsymbol{\phi}_{fp}$ are the mode shapes at the forced points “ fp ”, $f(\omega)$ is the vector of generalized, or modal forces, and $\psi(\omega)$ (equal to $[\mathbf{h}(\omega)f(\omega)]$) is the vector of modal amplitudes. Note that the response points need not be within the forced region of the structure.

The cross-power spectral density matrix of velocities at the response points is

$$G_{V_{rp}V_{rp}}(\omega) = 2 \lim_{T \rightarrow \infty} \frac{1}{T} \mathbf{E}[V_{rp}(\omega)V_{rp}^H(\omega)], \quad (10)$$

where $\mathbf{E}[\]$ is the expected value operator and the “ H ” superscript denotes the transpose and complex conjugate operations. Using some of the relations in Eq. (9), Eq. (10) may be expanded to

$$\begin{aligned} \mathbf{G}_{V_{rp}V_{rp}}(\omega) &= 2 \lim_{T \rightarrow \infty} \frac{1}{T} \mathbf{E} \left[\boldsymbol{\phi}_{rp}\mathbf{h}(\omega)\boldsymbol{\phi}_{fp}^T F(\omega) \left\{ \boldsymbol{\phi}_{rp}\mathbf{h}(\omega)\boldsymbol{\phi}_{fp}^T F(\omega) \right\}^H \right] \\ &= 2 \lim_{T \rightarrow \infty} \frac{1}{T} \mathbf{E} \left[\boldsymbol{\phi}_{rp}\mathbf{h}(\omega)\boldsymbol{\phi}_{fp}^T F(\omega) F^H(\omega) \boldsymbol{\phi}_{fp}^* \mathbf{h}^H(\omega) \boldsymbol{\phi}_{rp}^H \right] \\ &= \boldsymbol{\phi}_{rp}\mathbf{h}(\omega)\boldsymbol{\phi}_{fp}^T \mathbf{G}_{FF}(\omega) \boldsymbol{\phi}_{fp}^* \mathbf{h}^H(\omega) \boldsymbol{\phi}_{rp}^H, \end{aligned} \quad (11)$$

where $\mathbf{G}_{FF}(\omega)$ is the cross-power spectral density matrix of applied forces (in physical coordinates), and $*$ denotes complex conjugate. $\mathbf{G}_{FF}(\omega)$ may represent any form of distributed force, either deterministic or random. Eq. (11) is equivalent to Eq. (7), but in matrix form and based on modal, rather than physical, FRFs.

3.1.4. Generalized force cross-power spectral density matrices

Often the flow-induced fluctuating forces acting on structures have characteristic length scales much smaller than the wavelengths of the vibrations within the structural materials. In such cases, it is convenient to define a CSD matrix of generalized applied forces, where the CSD matrix of applied forces in physical coordinates is pre- and post-multiplied by a modal basis set defined over the loaded points f :

$$\mathbf{G}_{ff}(\omega) = \hat{\boldsymbol{\phi}}_{fp}^T \mathbf{G}_{FF}(\omega) \hat{\boldsymbol{\phi}}_{fp}^*. \quad (12)$$

Since in most cases the number of physical coordinates in a model far exceeds the number of modes used in a solution, $\mathbf{G}_{ff}(\omega)$ is usually of order much smaller than $\mathbf{G}_{FF}(\omega)$, greatly reducing computational resource requirements. Also, if the spatial resolution of the mode shapes $\boldsymbol{\phi}_{fp}$ is insufficient to resolve any fine-scale forces within $\mathbf{G}_{FF}(\omega)$, more refined mode shapes $\hat{\boldsymbol{\phi}}_{fp}$ may be generated by interpolating $\boldsymbol{\phi}_{fp}$ using spline functions. Therefore, $\mathbf{G}_{ff}(\omega)$ may be computed with accuracy without requiring excessive discretization of the structural–acoustic model (provided there is enough spatial resolution in $\boldsymbol{\phi}_{fp}$ such that the interpolated $\hat{\boldsymbol{\phi}}_{fp}$ are accurate).

3.1.5. Velocity spectra

To compute the velocity CSD matrix at all response points rp :

$$\mathbf{G}_{V_p V_p}(\omega) = \boldsymbol{\varphi}_{rp} [\mathbf{h}(\omega) \mathbf{G}_{ff}(\omega) \mathbf{h}^H(\omega)] \boldsymbol{\varphi}_{rp}^H = \boldsymbol{\varphi}_{rp} \mathbf{G}_{\psi\psi}(\omega) \boldsymbol{\varphi}_{rp}^H, \quad (13)$$

where $\mathbf{G}_{\psi\psi}(\omega)$ (equal to $[\mathbf{h}(\omega) \mathbf{G}_{ff}(\omega) \mathbf{h}^H(\omega)]$) is the CSD matrix of the mass-normalized modal amplitudes due to the applied force field. The terms in $\mathbf{G}_{\psi\psi}(\omega)$ have the units: $(\text{mass})(\text{length})^2/(\text{time})^2/\text{Hz} = (\text{mass})(\text{length})^2/(\text{time})$. To compute displacement or acceleration spectra, the velocity CSD matrix is simply divided or multiplied by factors of $i\omega$. For large problems, Eq. (13) represents an extremely efficient, compact approach to computing auto- and cross-power spectral densities at arrays of response points. $\mathbf{G}_{ff}(\omega)$, $\mathbf{h}(\omega)$, and $\mathbf{G}_{\psi\psi}(\omega)$ are all of order $M \times M$, where M is the number of modes included in the solution. The only vectors in physical coordinates are the mode shapes $\boldsymbol{\varphi}_{rp}$.

In restrictive cases, $\mathbf{G}_{\psi\psi}(\omega)$ is diagonal, implying no modal cross-coupling (the off diagonal entries in $\mathbf{G}_{\psi\psi}(\omega)$ are 0). This is only true in lightly damped systems, with widely spaced modes, and with negligible fluid-loading $\mathbf{Z}(\omega)$. Early analysis approaches (Powell, 1958, Wilby, 1967, Jacobs et al., 1970; Au-Yang and Connelly, 1977) assumed negligible modal cross-coupling, along with homogeneous applied pressure fields. All modal cross-coupling terms are considered in the approach described here, however, and inhomogeneous pressure fields, like those within fluid-filled piping elbows, are accounted for properly.

3.2. TBL flow excitation

Wall pressure fluctuations beneath turbulent boundary layers are partially correlated over space. Assuming a temporally stationary process, the cross-spectral density pressure excitation function $G_{p_i p_j}(\omega)$ may be separated into an averaged autospectral density function $\bar{\varphi}_{pp}(\omega)$ and a normalized cross-spectral density function $\Gamma(\Delta_1, \Delta_3, \omega)$ between the loaded points i and j :

$$G_{p_i p_j}(\omega) = \bar{\varphi}_{pp}(\omega) \Gamma(\Delta_1, \Delta_3, \omega) \cong \sqrt{\varphi_{p_i p_i}(\omega) \varphi_{p_j p_j}(\omega)} \Gamma(\Delta_1, \Delta_3, \omega), \quad (14)$$

where $\bar{\varphi}_{pp}(\omega)$ is approximated by the geometric mean of $\varphi_{p_i p_i}(\omega)$ and $\varphi_{p_j p_j}(\omega)$ and Δ_1 and Δ_3 are the streamwise and spanwise separation distances between points i and j . $G_{p_i p_j}(\omega)$ is multiplied by the incremental areas at points i and j to generate the entries of $\mathbf{G}_{FF}(\omega)$.

Many investigators have proposed empirical models of $\varphi_{pp}(\omega)$ and $\Gamma(\Delta_1, \Delta_3, \omega)$ for TBL flow fields with zero mean pressure gradient [see Hwang et al. (2003, 2009), Graham (1997) for summaries of some of the more popular models]. The models are effectively curve fits of measured data for geometrically similar flow fields, where the data are collapsed on the so-called inner, outer, or mixed flow variables. While the empirical models for wall pressure autospectra work well for uniform flows with no mean pressure gradients, they should not be used for complex flows like those within and downstream of piping elbows. Therefore, we apply a computational technique to calculate the wall pressure autospectra, and combine it with an empirical representation of $\Gamma(\Delta_1, \Delta_3, \omega)$.

3.2.1. Autospectra

The turbulent flow throughout the elbowed pipe was computed using CFD RANS with a Menter $\bar{k} - \bar{\omega} - \text{SST}$ turbulence model at two Reynolds numbers (based on pipe diameter): 2×10^6 , and 2×10^7 . This range of Reynolds numbers encompasses a wide range of flow speeds, pipe diameters, and viscosities. The CFD grid was sublayer-resolved to a dimensionless distance y^+ of 1 to capture small length scales in the flow turbulence and corresponding mid- to high-frequency content in the wall pressure fluctuations. Using the TBL forcing function (TBLFF) methods described by Peltier and Hambric (2007), the turbulence and velocity distributions through the flow profiles were integrated to compute autospectra of the wall pressure fluctuations. In Hambric et al. (2003), similar calculations for a slightly different elbow (and lower Reynolds number flow) were validated against measured data, particularly in regions where the flow is subjected to adverse and favorable pressure gradients.

The estimated wall pressure autospectra over the full elbowed pipe are shown in Fig. 4 for low frequencies. The contour levels are non-dimensionalized using outer flow variables (displacement thickness δ^* and bulk velocity U_o), and plotted at a low dimensionless frequency ($\omega \delta^* / U_o$) of 0.1. As shown in Fig. 5, the dimensionless pressure spectra at the inlet generally match those of similar flows through straight pipes reported previously (Keith et al., 1992) for both outer and mixed variable scaling, providing additional confidence in the forcing function simulation procedure. However, at higher dimensionless frequencies ($\omega \delta^* / U_o > 2$), the simulated pressure levels exceed those measured previously [the measured pressures include the usual Corcos corrections for sensor surface area attenuation effects Corcos (1963)]. Earlier TBLFF simulations of wall pressure autospectra are also biased slightly high at higher frequencies, particularly

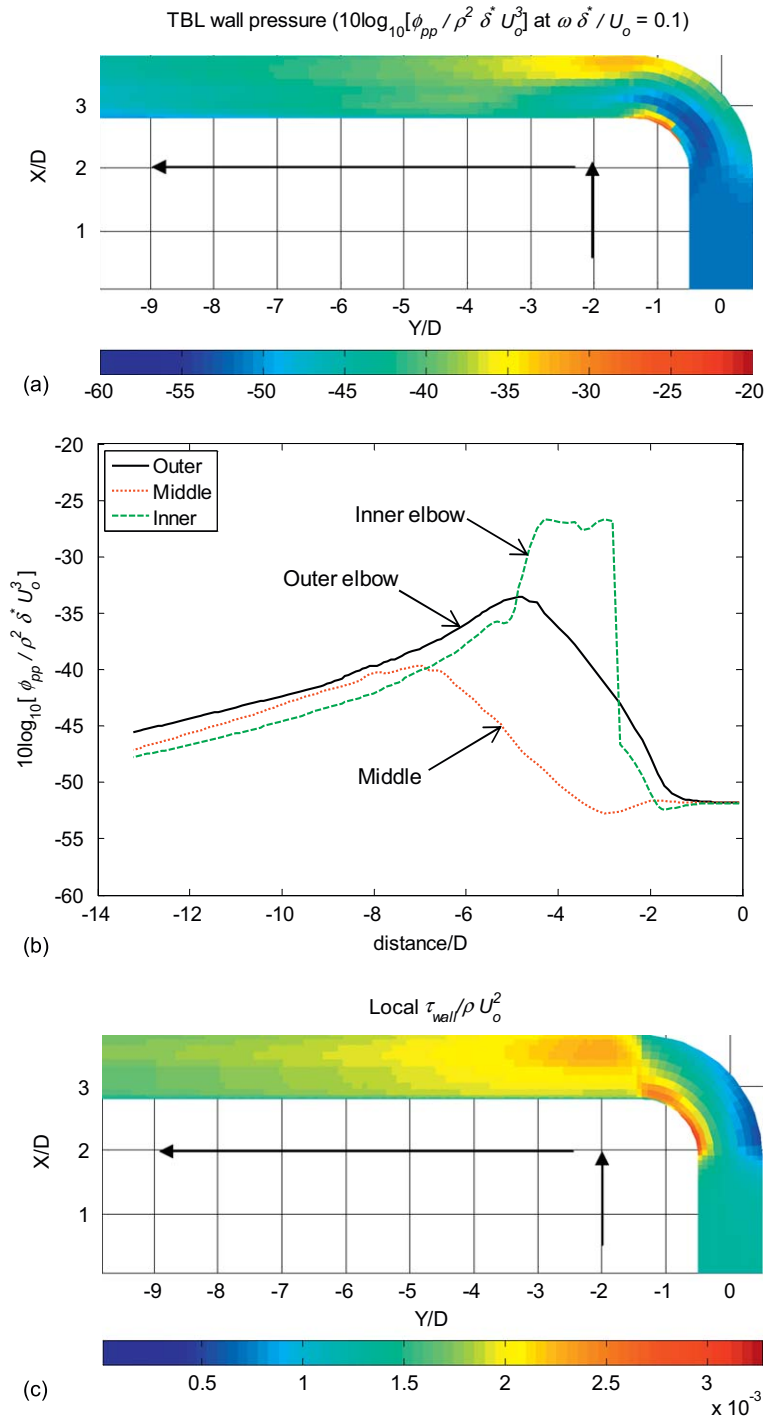


Fig. 4. (a) Wall pressure distribution in TBL-excited piping system with 90° elbow, inlet at lower right, discharge at upper left; (b) wall pressures along pipe from inlet ($d/D = 0$) to discharge ($d/D \sim 13.5$); (c) local wall shear stress normalized by density and bulk velocity. Contours are of TBL wall pressure one-sided autospectral densities are scaled on outer flow variables at dimensionless frequency $\omega \delta^*/U_o = 0.1$, $Re_D = 2 \times 10^6$.

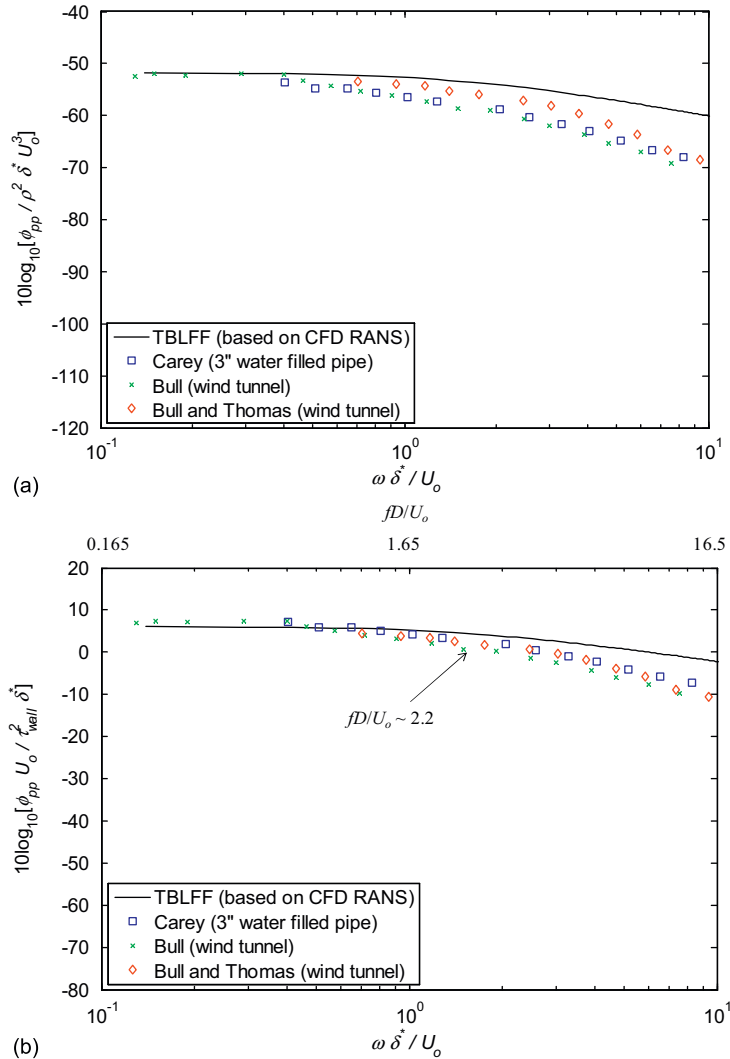


Fig. 5. Piping inlet TBL wall pressure autospectrum, scaled on (a) outer and (b) mixed variables, compared with scaled historical measurements listed in Keith et al. (1992).

for flows with favorable pressure gradients. We address this high frequency bias further when presenting our final results later in this paper.

Fig. 4 shows that the pressure levels on and downstream of the outer elbow surface are significantly higher than those within the inlet, particularly along the outer surface. The increase in fluctuating pressure is caused by gradients introduced into the flow by the elbow, and by corresponding increases in turbulence intensity. We note that the effects of the elbow on wall pressure amplitude continue well downstream of the elbow. Therefore, we consider the wall pressure fluctuations which span the elbow itself, along with the excitation one diameter upstream and four diameters downstream of the elbow joints.

Increasing Reynolds number generally decreases scaled (dimensionless) wall pressure fluctuation amplitudes (along with other related parameters, like scaled wall shear stress and scaled friction velocity). The CFD RANS/TBLFF simulations of wall pressure autospectral amplitudes over the elbow (and one diameter upstream and four diameters upstream of the elbow) are compared for Re_D of 2×10^6 , and 2×10^7 and scaled on outer variables in Fig. 6. As expected, the scaled wall pressure levels decrease slightly with increasing Reynolds number.

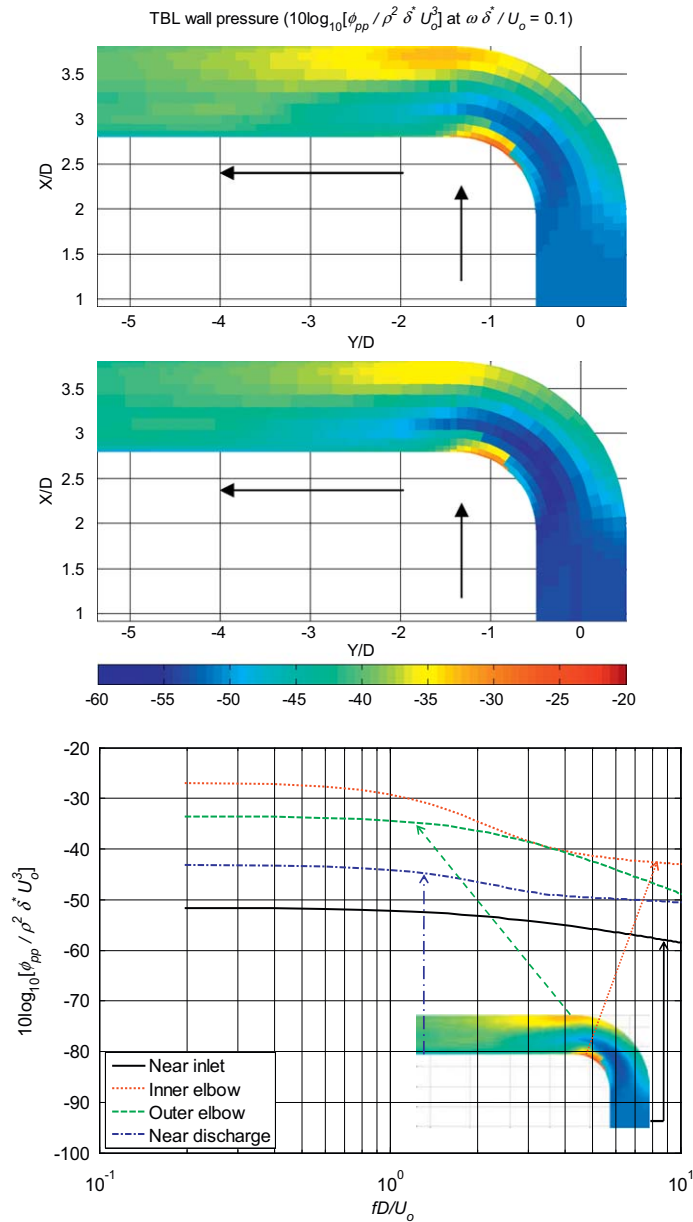


Fig. 6. TBL dimensionless wall pressure one-sided autospectral densities over excited region only (one diameter upstream and four diameters downstream of elbow), scaled on outer flow variables, at dimensionless frequency $\omega\delta^*/U_0 = 0.1$, $Re_D = 2 \times 10^6$ (top), $Re_D = 2 \times 10^7$ (middle). Bottom – TBL wall pressure autospectra at four locations for $Re_D = 2 \times 10^6$.

3.2.2. Cross-spectra

Since the TBL wall pressures are random over space, a cross-spectral model for $\Gamma(\Delta_1, \Delta_3, \omega)$ is required to complete the definition of the loading function $\mathbf{G}_{FF}(\omega)$. $\Gamma(\Delta_1, \Delta_3, \omega)$ may be viewed as a normalized cross-spectral function of the fluctuating wall pressures, such that

$$\Gamma(\Delta_1, \Delta_3, \omega) = \frac{1}{2\pi} \int_{-\infty}^{\infty} \rho(\Delta_1, \Delta_3, \tau) e^{i\omega\tau} d\tau, \tag{15}$$

where ρ represents the normalized cross-covariance of the fluctuating pressure field (assumed locally homogeneous) and Γ depends only on frequency and the separation vector (Δ_1, Δ_3) between points i and j in the plane of the flow. Several investigators have assumed that $\Gamma(\Delta_1, \Delta_3, \omega)$ may be separable in the streamwise and spanwise flow directions, including Corcos (1963), who proposed the well-known model:

$$\Gamma(\Delta_1, \Delta_3, \omega) = A(\omega\Delta_1/U_c)B(\omega\Delta_3/U_c), \quad (16)$$

where U_c is the average convection velocity of the flow, which is some fraction of the free stream velocity U_o .

The convection velocity may be approximated using the empirical formula from Bull (1967) as a function of ω , U_o , and δ^* :

$$U_c \cong U_o(0.59 + 0.30e^{-0.89\omega\delta^*/U_o}). \quad (17)$$

Corcos postulated that the functions A and B may be represented as an exponentially decaying oscillating function in the flow direction and a simple exponentially decaying function in the cross-flow direction:

$$A(\omega\Delta_1/U_c) = e^{-\alpha_1|\omega\Delta_1/U_c|}e^{i\omega\Delta_1/U_c}, \text{ and } B(\omega\Delta_3/U_c) = e^{-\alpha_3|\omega\Delta_3/U_c|}, \quad (18a, b)$$

where α_1 and α_3 are decay constants in the streamwise and cross-flow directions, respectively. The decay terms may be viewed as separation distances Δ normalized by the effective correlation lengths of the wall pressures, $U_c/\omega\alpha$. The oscillating term $e^{i\omega\Delta_1/U_c}$ represents the pressure pulsations convecting over the surface. However, for low speed flows the bending waves in the excited structure are so large with respect to the convective pressure fluctuations that the oscillating term may be ignored (Hambric et al., 2003, 2004). In these cases, the structure acts as a filter, rejecting the convective excitation. The remaining portion of the excitation field $\Gamma(\Delta_1, \Delta_3, \omega)$ is termed the “low wavenumber region”, which coincides with the structural vibration wavenumbers.

Eq. (18) usually overestimates the low-wavenumber region of the TBL wall pressures. Ko (1991) and Hwang et al. (2003) have evaluated a modification to the Corcos model, where

$$A(\omega\Delta_1/U_c) = (1 + \alpha_1|\omega\Delta_1/U_c|)e^{-\alpha_1|\omega\Delta_1/U_c|}e^{i\omega\Delta_1/U_c}. \quad (19)$$

Pre-multiplying the original Corcos A function by $(1 + \alpha_1|\omega\Delta_1/U_c|)$ shifts more of the energy in the wall pressure field into the convective region, reducing pressure amplitudes in the low-wavenumber region.

To remove the convective terms from Eq. (19), Hwang transforms the equation into wavenumber–frequency space, truncates the resulting spectrum at a cutoff wavenumber k_p , and inverse transforms the result back into physical coordinates. The result,

$$\Gamma(\Delta_1, \Delta_3, \omega) = \left(\frac{2\alpha_1^3}{\pi^2\alpha_3}\right)\left(\frac{k_p}{k_c}\right)^2\left(2\pi\frac{J_1(k_p|\Delta|)}{k_p|\Delta|}\right), \quad (20)$$

where Δ is the separation vector between loaded points and k_c is ω/U_c , may be readily applied to finite element models. For the smooth walls in the examples considered here, we set α_1 to 0.1, and α_2 to 0.7. However, note that α_1 can increase significantly for flow over rough walls (Blake, 1970), reducing the streamwise correlation lengths, and increasing the low-wavenumber levels.

Fig. 7 shows examples of the Hwang low-wavenumber forcing function in dimensionless wavenumber space (left) and in physical coordinates (right) relative to a reference point on the pipe. The model only includes low-wavenumber terms up to a dimensionless wavenumber of $k_p U_c/\omega$. We choose $k_p = 40$ based on our assumption that $k/k_c < 0.1$. The low-wavenumber model, when exercised with an appropriate k_p ,¹ leads to oscillations in the pressure excitation that are long with respect to the structural dimensions, as shown in Fig. 7. Also, there is no frequency dependence in the oscillating term of the model (there is frequency dependence in its amplitude, however, based on k_c and the autospectrum). Finally, leakage effects due to truncating the forcing functions at the ends of the pipes, which can be substantial when including high-wavenumber convective terms, are minimal with the low-wavenumber model.

3.2.3. Boundary layer edge velocities and displacement thicknesses

To use Bull’s approximation for convection velocity, the local free-stream velocity and boundary layer displacement thickness are required. For flat plate boundary layer flow, these quantities may be estimated with reasonable accuracy

¹A large k_p may be chosen, but would not improve model accuracy. Large k_p values would decrease the oscillation lengths in the J_1 term, increasing the mesh density requirements of the underlying structure. k_p should therefore be chosen large enough to encompass the wavenumber content of the structural vibrations, but no larger.

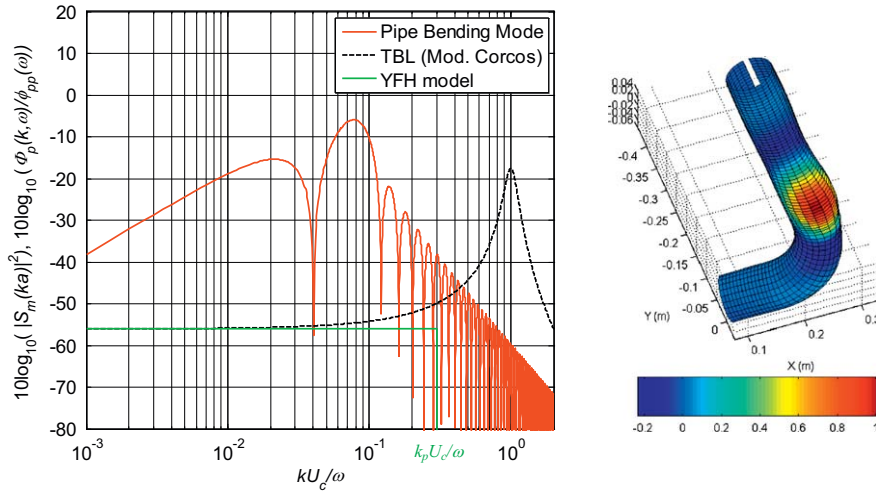


Fig. 7. Left: Hwang’s low-wavenumber cross-spectral model (in green) compared with a modified Corcos model and the wavenumber transform of a pipe structural mode; Right: example of $J_1(k_p|\xi|)/k_p|\xi|$ over pipe elbow for a given reference location (the reference location has an amplitude of 1) (For interpretation of the references to colour in this figure legend, the reader is referred to the web version of this article.)

from the CFD solutions. For straight pipe flow, the free stream velocity is simply that at the pipe center, and the boundary layer displacement thickness can be estimated as a fraction of the pipe radius. For the flow fields within and downstream of the elbow, however, the quantities are not easily defined.

We apply a technique based on Menter’s (1992, 1994) blending function, which is used to define transition regions between two-layer turbulence models, to find automatically the localized boundary layer edges throughout the pipe flow, along with approximate boundary layer thicknesses. We assume the location of the transition region defines the effective boundary layer limit, and therefore the equivalent freestream, or “edge” velocity. Appendix A provides a detailed description of the procedure.

Boundary layer displacement thickness is defined as the distance by which the solid boundary would have to be displaced in a frictionless flow to give the same mass flow rate deficit as exists in the boundary layer, so

$$\delta^* = \int_0^\infty \left(1 - \frac{u}{U_{\text{edge}}}\right) dy \approx \int_0^\delta \left(1 - \frac{u}{U_{\text{edge}}}\right) dy, \quad (21)$$

where y is the distance normal to the wall, u the local component of the velocity tangential to the wall, U_{edge} the edge velocity, and δ the disturbance thickness, usually defined as the distance from the surface to the point where the velocity is within 1% of the edge velocity.

Figs. 8 and 9 show the inferred displacement thickness and free stream velocity distributions over the pipe elbow at $\text{Re}_D = 2 \times 10^6$. The displacement thickness of the inflow (fully developed straight pipe flow) is about 1/9th of the diameter, and decreases within and downstream of the elbow. The boundary layer edge velocity is about 20% higher than the bulk velocity at the elbow inlet, and decreases on the outer elbow surface, and on the inner pipe surface downstream of the elbow.

3.3. Structural–acoustic response of finite structure and fluid regions

3.3.1. FE model

The motion of waves propagating along a pipe can be described as a series summation over all circumferential harmonics, where

$$w(\theta, z, t) = \left(\sum_{n=1}^{\infty} W_n \cos(n\theta) + \sum_{n=1}^{\infty} V_n \sin(n\theta) \right) e^{-ik_z z + i\omega t}. \quad (22)$$

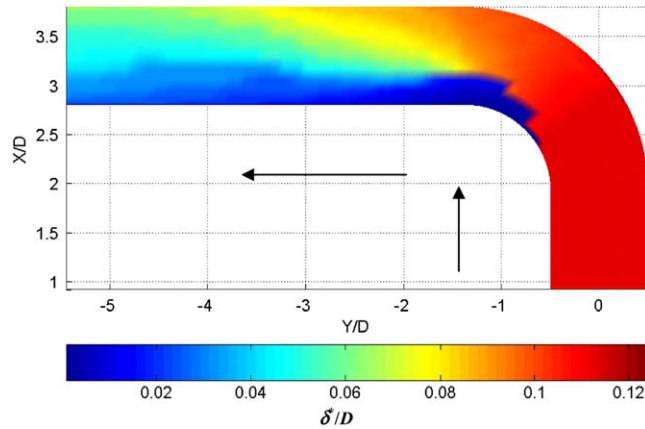


Fig. 8. Approximate displacement thickness over excited region (one diameter upstream and four diameters downstream of elbow), normalized by diameter, $Re_D = 2 \times 10^6$.

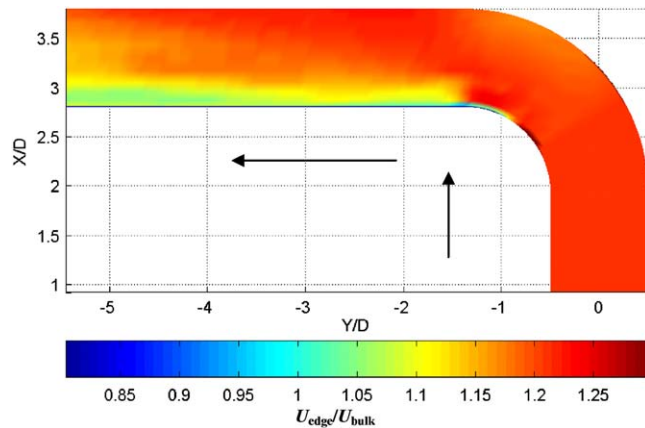


Fig. 9. Approximate boundary layer edge velocity over excited region (one diameter upstream and four diameters downstream of elbow), normalized by bulk velocity, $Re_D = 2 \times 10^6$.

As various circumferential harmonics n cut on with increasing frequency, the vibrations of the wall become more complex. For the pipes and frequencies considered here, n is limited to 3.

An FE model of the piping walls was constructed using shell elements, which represent both plate and membrane waves, including their coupling through the wall curvature. The model is used for analyses of both the Schedule 10 (3.05 mm [0.12 in] wall thickness) and Schedule 40 (5.49 mm [0.216 in] wall thickness) pipes. Based on the CFD-simulated wall pressures, a section of the pipe extending one diameter upstream and four diameters downstream of the elbows is modeled, as shown in Fig. 10. Models of thin, rigid, massless pistons were added to the inlet and discharge of the truncated pipe. The pistons are used to couple a boundary element model of the internal fluid acoustic impedance to the walls of the structural FE model and to the impedances of the upstream and downstream fluid columns.

Normal modes for the Schedules 10 and 40 truncated pipes were computed for frequencies of resonance up to 8 kHz. 75 modes were extracted for the Schedule 10 piping and 51 for the Schedule 40 piping. Eight rigid body modes were included in each of the mode sets. Table 1 lists the cut-on frequencies for $n = 2$ and 3 circumferential mode orders for the piping. The mode sets also include beam ($n = 1$) modes, and torsional modes of the respective legs. No purely axial modes were found below 8 kHz for either pipe, but axial motion of both the inlet and discharge legs is observed in many of the flexural pipe modes. Fig. 11 shows how bending motion in one of the legs couples to torsional or axial motion in the other leg. This means that the pressures induced by the TBL flow, which are normal to the walls, will cause flexural, as well as axial and torsional motion in the legs upstream and downstream of the elbow.

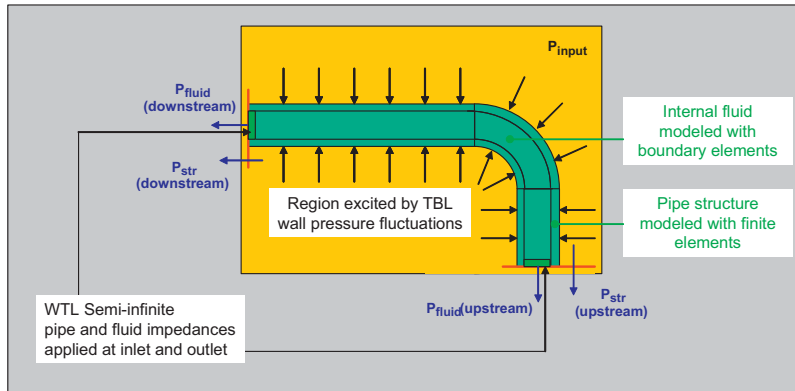


Fig. 10. Loaded region of pipe with elbow.

Table 1
FE cuton frequencies (Hz) for Schedules 10 and 40 steel 3 in piping.

	$n = 2$	$n = 3$
Schedule 10	1022	2943
Schedule 40	1932	5641

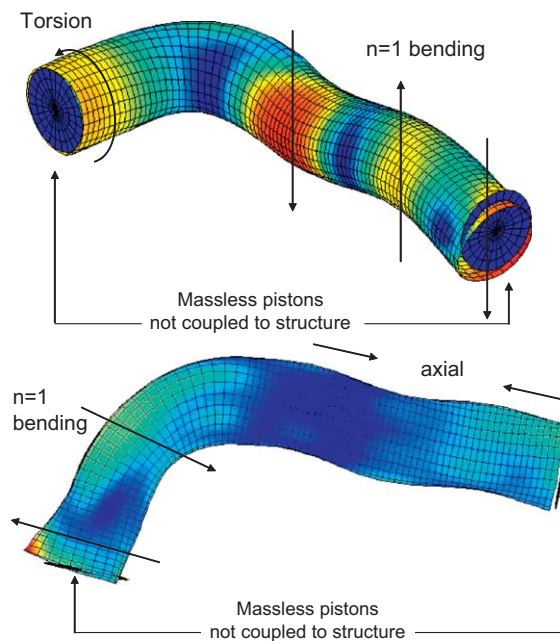


Fig. 11. In-vacuo FE modes of loaded region of Schedule 10.3 in steel pipe with 90° elbow; $n = 1$ out-of-plane bending coupled to torsion in inlet (top) and $n = 1$ in-plane bending coupled to axial motion in outlet (bottom).

3.3.2. BE model

A BE model of the fluid within the loaded region of the piping elbow was generated with the lumped parameter software POWER (Fahnline and Koopmann, 1996, 1997; Koopmann and Fahnline, 1996; Fahnline, 2009). The BE model was linked not only to the structural walls, but also to the rigid massless pistons at the ends of the pipe. A slip condition between the pistons and the elbow inlet and outlet is enforced, such that the pistons only move in the

direction of plane wave propagation in the fluid. This approach allows structural wall motion to couple to the pistons via the BE fluid model. If the pistons are also connected to external fluid impedances, such as those within the fluid in connected piping, or an infinite baffled or unbaffled body of fluid, they can radiate sound power. This will be demonstrated later in the results section, where acoustic sound power levels are compared with structure-borne sound.

3.4. Semi-infinite structure and fluid regions

The ends of the loaded pipe region shown in Fig. 10 are coupled to impedances of structural and acoustic wavetypes in semi-infinite piping and fluid. For frequencies below 5 kHz, the following waves can propagate in Schedules 10 and 40 76.2 mm (3 in) piping: (i) axial ($n = 0$), (ii) torsional ($n=0$), (iii) flexural ($n=1, 2$, and 3), and (iv) fluid ($n=0$, or plane-waves), where flexural waves propagate along two planes – in and out of the plane of the elbow. The infinite impedances draw fluid- and structure-borne powers away from both ends of the elbow.

The impedances of the axial and fluid waves ($n = 0$) in a semi-infinite pipe are computed easily as

$$Z = \rho c A, \quad (23)$$

where ρ is mass density, c the speed of sound of the wavetype, and A the area of the cross-section (of the fluid or structure). The axial waves in the pipe walls propagate at a sound speed of $\sqrt{E/\rho_s}$, where E is Young's modulus and ρ_s is structural density. For the fluid waves, we assume an acoustic wavespeed c_o in water of 1500 m/s and a mass density ρ_o of 1025 kg/m³.

The semi-infinite impedance of torsional waves in pipe walls is

$$Z_{\text{torsional}} = \rho_s J c_s / a^2, \quad (24)$$

where J is the polar moment of inertia of the cross-section, c_s the shear wavespeed of the wall material ($\sqrt{G/\rho_s}$), G shear modulus, and a the mean radius of the wall.

The semi-infinite impedances of the bending waves in pipes are not computed as easily as those of axial and torsional waves. At low frequencies, semi-infinite beam impedances represent the $n = 1$ flexural impedances of the pipes, where

$$Z_{\text{beam}} = \frac{1}{2} \rho_s A_s c_B (1 + i), \quad (25)$$

where c_B is the bending wavespeed in a beam. The rotational, or moment impedance of $n = 1$ flexural waves is $k_B^2 Z_{\text{beam}}^*$, where “*” denotes the complex conjugate.

At and above the cut-on frequency of lobar ($n > 1$) modes in the piping walls, the semi-infinite flexural impedances cannot be computed in closed form. The wave transmission line (WTL) modeling approach described by Stokes et al. (2001) may be used to compute the flexural (and axial and torsional) impedances based on dispersion relationships between wavetypes. The dispersion relationships are based on the Donnell–Mushtari thin shell theory augmented with a Flugge–Lur'ye–Byrne modifier to represent thick shell effects (Leissa, 1993). Internal acoustic fluid is coupled to the shell by enforcing continuity of velocity at the wall.

The WTL may be used to generate complete frequency-dependent matrices of semi-infinite pipe impedances for each circumferential harmonic of interest, including coupling between wavetypes. To couple the WTL impedances, which are computed for individual circumferential harmonics, to the FE and BE models of the pipe, which are modeled in physical coordinates, the FE mode shapes at the pipe ends must be decomposed into their circumferential harmonics for radial, circumferential, and axial motion. The WTL impedances are then converted into modal coordinates and included in the coupled FE/BE/WTL solution via the $\mathbf{c}(\omega)$ matrix in Eq. (8).

3.5. Power input to semi-infinite wave impedances

ARL/Penn State's CHAMP approach is used to compute the structure- and fluid-borne power emanating from the ends of the TBL-excited elbow. Recall from Section 3.1.1 that

$$\mathbf{h}(\omega) = i\omega [-\omega^2 \mathbf{m} - i\omega \mathbf{b} + \mathbf{k} + \mathbf{z}(\omega) + \mathbf{c}(\omega)]^{-1}. \quad (26)$$

The internal fluid impedances and WTL semi-infinite pipe impedances are coupled to the pipe structure via the $\mathbf{z}(\omega)$ and $\mathbf{c}(\omega)$ matrices, respectively. $\mathbf{h}(\omega)$ is then computed for all frequencies of interest (we choose 1/3-octave band frequencies between 250 and 5000 Hz here). Once the modal response coefficients $\mathbf{G}_{\psi\psi}(\omega)$ are known, the power injected into the attached semi-infinite pipe impedances may be computed as a summation over

the modal coefficient matrices:

$$G_{P_{\text{attached}}}(\omega) = \sum_{m=1}^M \sum_{n=1}^M \text{Re}[c_{mn}(\omega)] G_{\psi_m \psi_n}(\omega), \quad (27)$$

for each wavetype and circumferential harmonic, including both structural and acoustic waves.

4. Results

4.1. Unscaled power inputs to structural and fluid waves

The power transmitted into the pipes upstream and downstream of the elbow of the Schedule 10 76.2 mm (3 in) water-filled steel pipe for TBL flow at a bulk velocity of 21 m/s and a Re_D of 2×10^6 is shown in Fig. 12. The in-plane and out-of-plane (cosine and sine) components of $n = 1$ flexural powers are similar, and are summed in the plots for brevity. The power is highest at low frequencies, where the TBL wall pressure amplitudes are highest, and the correlation lengths ($U_c/\omega\alpha_i$) of the wall pressures are long (correlation lengths decrease with increasing frequency).

In general, the power levels in the flexural waves are higher than those in other wavetypes, since the TBL excitation acts in the radial direction, directly exciting flexural motion. The flexural powers downstream of the elbow are particularly high. The $n = 2$ flexural waves have high power levels near their cut-on frequency (~ 800 Hz). The coupling between structural wavetypes induced by the elbow (recall Fig. 11) is evident in the high power levels in axial waves at low frequencies (especially in the upstream direction), and modest power levels in torsional waves at high frequencies. At high frequencies, the power is partitioned nearly equally between structural wavetypes. Flexural motion of the pipe walls also couples weakly to acoustic waves, leading to relatively low power levels in the entrained fluid.

CHAMP was exercised on other pipe and flow configurations. Fig. 13 compares the power in upstream waves for flow velocities of 21 and 105 m/s for the Schedule 10 76.2 mm (3 in) water filled pipe. Flow speed has a strong effect on power levels, since it has a correspondingly strong effect on the amplitudes of TBL wall pressure fluctuations. Increasing flow speed also increases correlation lengths of the turbulence acting over the pipe surface.

The effects of increasing Reynolds number on power emanating upstream of the elbow of the water-filled Schedule 10 76.2 mm (3 in) pipe excited by turbulent flow traveling at 21 m/s are shown in Fig. 14. The increased Reynolds number condition may be viewed as a decrease in kinematic viscosity. Since increasing Reynolds number decreases wall pressure fluctuation amplitudes slightly, it also decreases power levels in all wavetypes. The Reynolds number effects are weak compared with those of flow speed, however.

Finally, we evaluate the effects of piping wall thickness on power spectra in Fig. 15, which shows that power levels decrease in Schedule 40 pipe (which has about double the wall thickness of Schedule 10 pipe). The increased wall

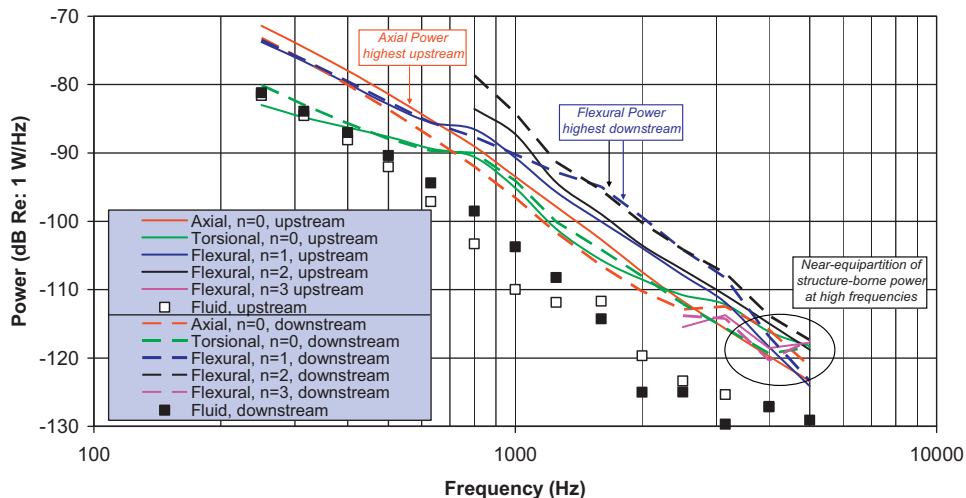


Fig. 12. Simulated (CHAMP) power emanating from TBL-excited Schedule 10 water-filled 76.2 mm (3 in) steel elbow, $U = 21$ m/s, $\text{Re}_D = 2 \times 10^6$, in upstream and downstream directions.

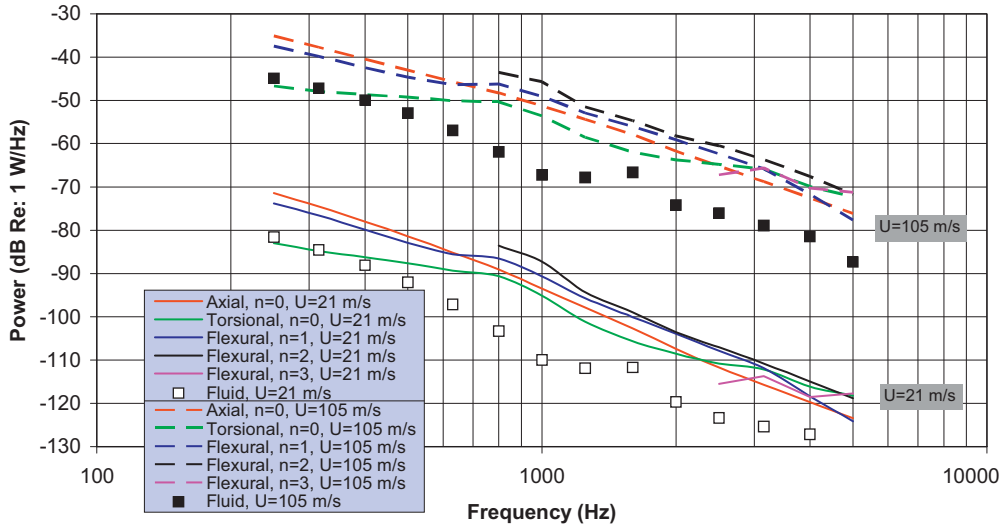


Fig. 13. Simulated power emanating from TBL-excited Schedule 10 water-filled 76.2 mm (3 in) steel elbow, $Re_D = 2 \times 10^6$, in upstream direction, for bulk flow velocities of 21 and 105 m/s.

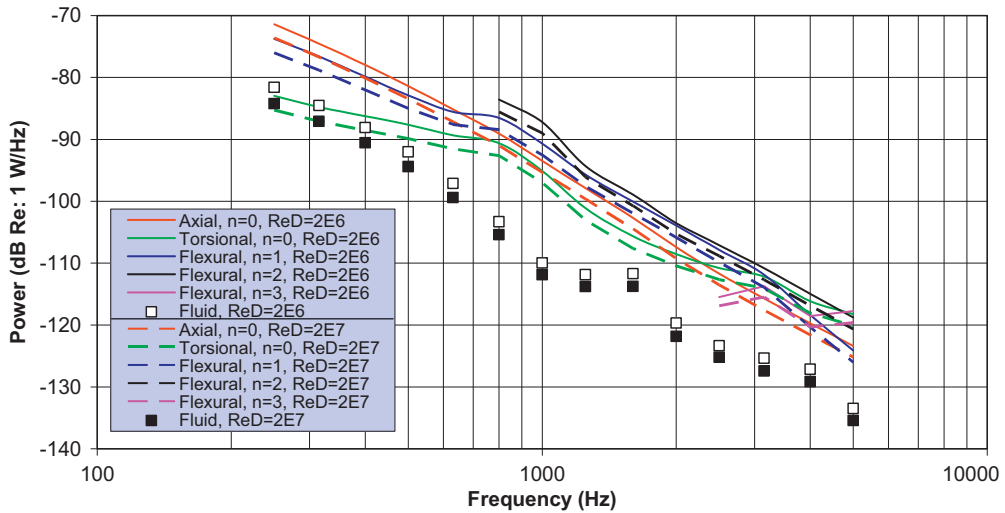


Fig. 14. Simulated power emanating from TBL-excited Schedule 10 water-filled 76.2 mm (3 in) steel elbow, $U = 21$ m/s, in upstream direction, for $Re_D = 2 \times 10^6$ and 2×10^7 .

thickness increases the impedance of the structure, reducing its acceptance of the TBL excitation energy. Also, the increased wall thickness increases the cuton frequencies of the $n = 2$ and 3 flexural waves. In fact, the $n = 3$ modes in the Schedule 40 pipe cut on at the upper limit of the analysis frequency range (5 kHz).

4.2. Scaling of power inputs

The power spectra for all wavetypes in the upstream direction are summarized in Fig. 16 for variable flow speed, Reynolds number, and pipe wall thickness. For the spectra to be useful to the practicing engineer, some sort of scaling must be used to collapse the data. Once a reasonable scaling is determined, empirical functions may be fit to the collapsed data so that approximate power spectra may be inferred for other geometrically similar pipes (such as those with larger diameters or different working fluids, for example).

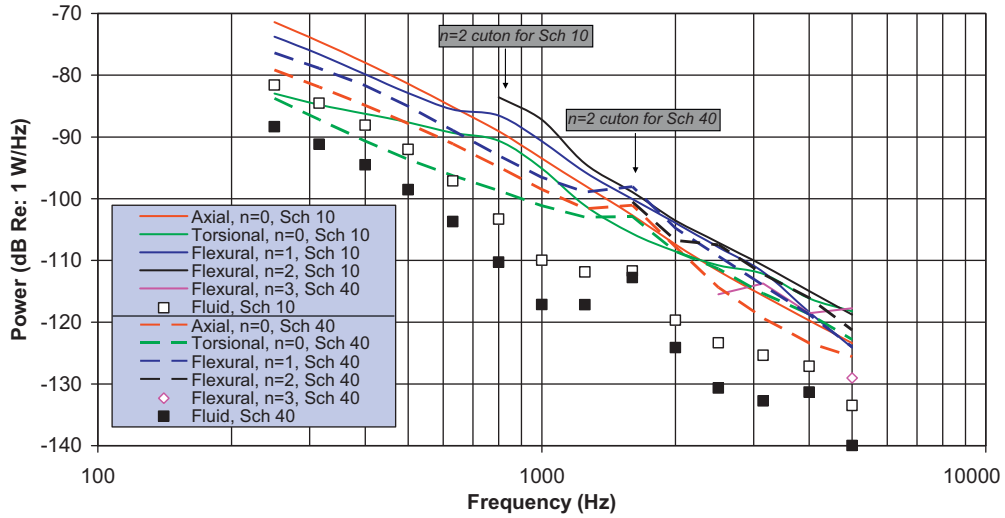


Fig. 15. Simulated power emanating from TBL-excited water-filled 76.2 mm (3 in) steel elbow, $Re_D = 2 \times 10^6$, $U = 21$ m/s, in upstream direction, for Schedule 10 and 40 pipe.

The power in a given wavetype at a particular frequency is proportional to $G_{FF}H_{v/F}$, where G_{FF} is the spectral density of wall force fluctuations and $H_{v/F}$ is the mobility of the wall (and connected structures and fluid). G_{FF} is the product of the wall pressure autospectrum and the regions over which the pressures are correlated. Therefore, parameters proportional to the wall pressures, surface area, and structural–acoustic mobility are required to properly scale the power spectra. Since perfect scaling of the results is not practical for a complex system, we offer instead an empirical scaling approach based on dimensional and physical analysis of the fluid flow and piping.

Wall pressure autospectra may be scaled using different flow variables (Keith et al., 1992). Outer variables, which depend on large-scale flow parameters, work best for the low-frequency range. Therefore, the outer variables U_o (bulk velocity), D (pipe diameter), and ρ_o (fluid mass density) are used to scale the wall pressures since high frequency wall pressure fluctuations are not likely to be significant noise sources for TBL flow excitation. Wall pressure spectra are also scaled against a non-dimensional frequency, in this case fD/U_o , which we will also use as a non-dimensional frequency for the power spectra. The region of excitation is proportional to the pipe circumference πD and axial length of the elbow L , and also to the decay coefficients α_1 and α_3 (which are included in the cross-correlation model in Eq.(20)). Finally, the fluctuating velocities, stresses, and wall pressures in a wall-bounded turbulent flow field depend weakly on Reynolds number. The literature on turbulent flat plate, channel, and pipe flow includes a range of Reynolds number dependencies (usually of wall shear stress or friction velocity). For the RANS model used here, an exponent of 1/7th works well, and is within the range of values reported by Burmeister (1993). Combining the wall pressure outer variable scaling, the (weak) Reynolds number dependence, and the decay coefficients and excited region, the power is multiplied by the factor $\alpha_3 Re_D^{1/7} / (\alpha_1^3 \rho_{fluid}^2 U_o^3 D_{pipe}^3 L_{elbow}^2)$.

To scale structural mobility, we use combinations of localized and semi-infinite mobilities. Consider that each localized wall pressure source “sees” a combined impedance (inverse of mobility), consisting of local flexural impedances and remote (at elbow ports) wavetype impedances. For example, local flexural waves in the wall couple to torsional and axial semi-infinite waves at both the upstream and downstream ends. Also, local flexural waves in the wall couple to internal fluid waves, which in turn couple to semi-infinite fluid columns attached to the upstream and downstream ends. For our scaling, we therefore combine localized flexural impedances with semi-infinite impedances of axial, torsional, and fluid waves, but use only flexural impedance to scale flexural powers. The parameters from the infinite beam flexural, axial, and torsional impedances discussed previously are combined with the forcing function parameters described above to complete the scaling of powers (note that we multiply power by impedance, which is the same as dividing by mobility):

$$G_{power_{scaled}} \text{ (dB)} = 10 \log_{10} G_{power_{wavetype}} + 10 \log_{10} \left[\left(\sum Z_{wavetype(s)} \right) \alpha_3 Re_D^{1/7} / (\alpha_1^3 \rho_{fluid}^2 U_o^3 D_{pipe}^3 L_{elbow}^2) \right]. \quad (28)$$

For flexural powers, $\sum Z_{wavetype(s)}$ is simply the flexural impedance of an infinite beam (amplitude of Eq. (25), without the factor of 1/2). For axial and torsional powers, $\sum Z_{wavetype(s)}$ is the sum of the flexural impedance of an infinite beam and semi-infinite axial (Eq. (23)) and torsional (Eq. (24)) waves. For acoustic powers, the flexural impedance is summed

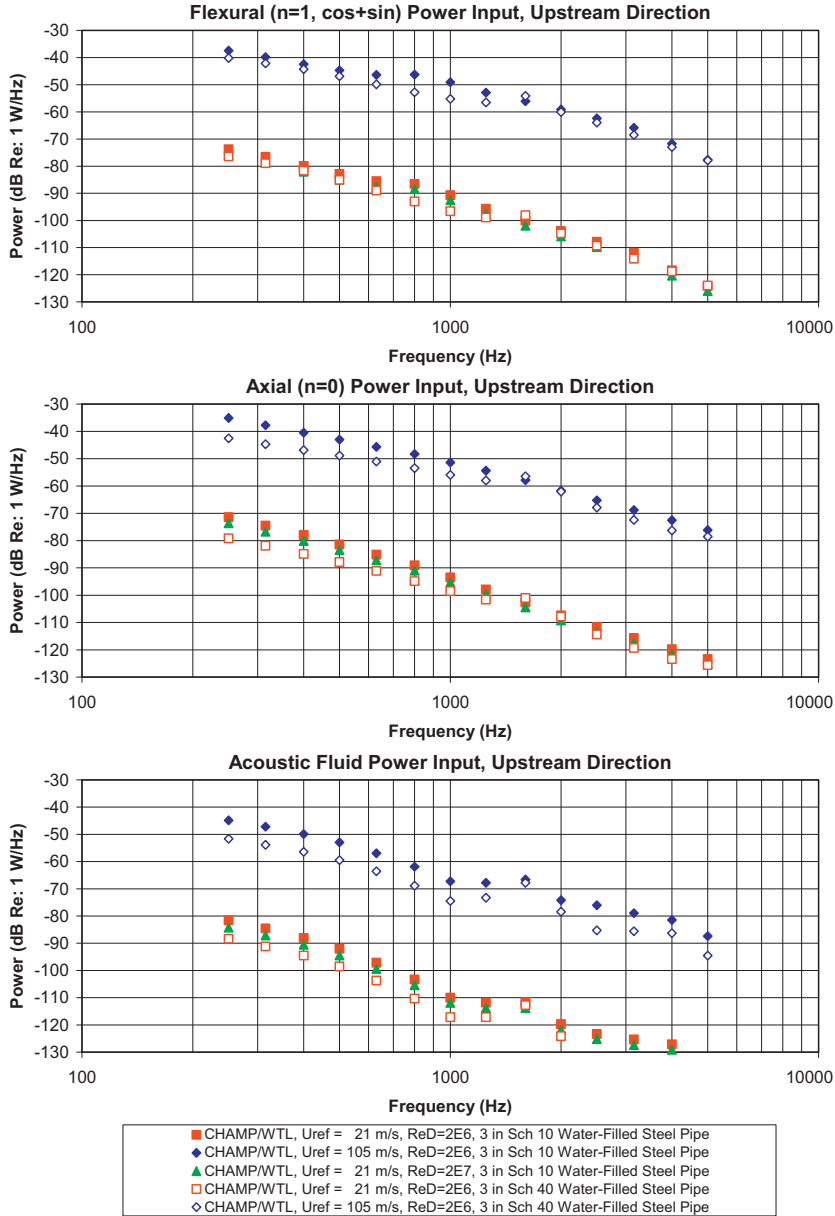


Fig. 16. Simulated power in $n = 1$ flexural (top), axial (middle), and acoustic (bottom) waves emanating from TBL-excited water-filled 76.2 mm (3 in) steel elbows, in upstream direction, for two different flow speeds, pipe Schedules, and Reynolds numbers.

with a portion of the acoustic impedance (Eq. (23)), where

$$\sum Z_{\text{wavetype}(s)} = Z_{\text{beam}} + (\rho_s A_s / \rho_o A_o)^2 Z_{\text{fluid}}. \quad (29)$$

The coupling factor between the pipe walls and internal fluid, $(\rho_s A_s / \rho_o A_o)^2$, is a low-order approximation. A more rigorous, frequency and wavenumber dependent coupling factor is available in Stokes et al. (2001), but would be quite difficult to apply to a general, simplified power scaling.

Fig. 17 shows the powers in flexural ($n = 1$), axial ($n = 0$), and acoustic ($n = 0$) waves in the upstream direction, scaled using Eq. (28) (the collapse and trends for other wavetypes, and in the downstream direction, are similar to those shown in Fig. 17). Recall that the scaled power spectra are plotted against a dimensionless frequency fD/U_o . The scaled data

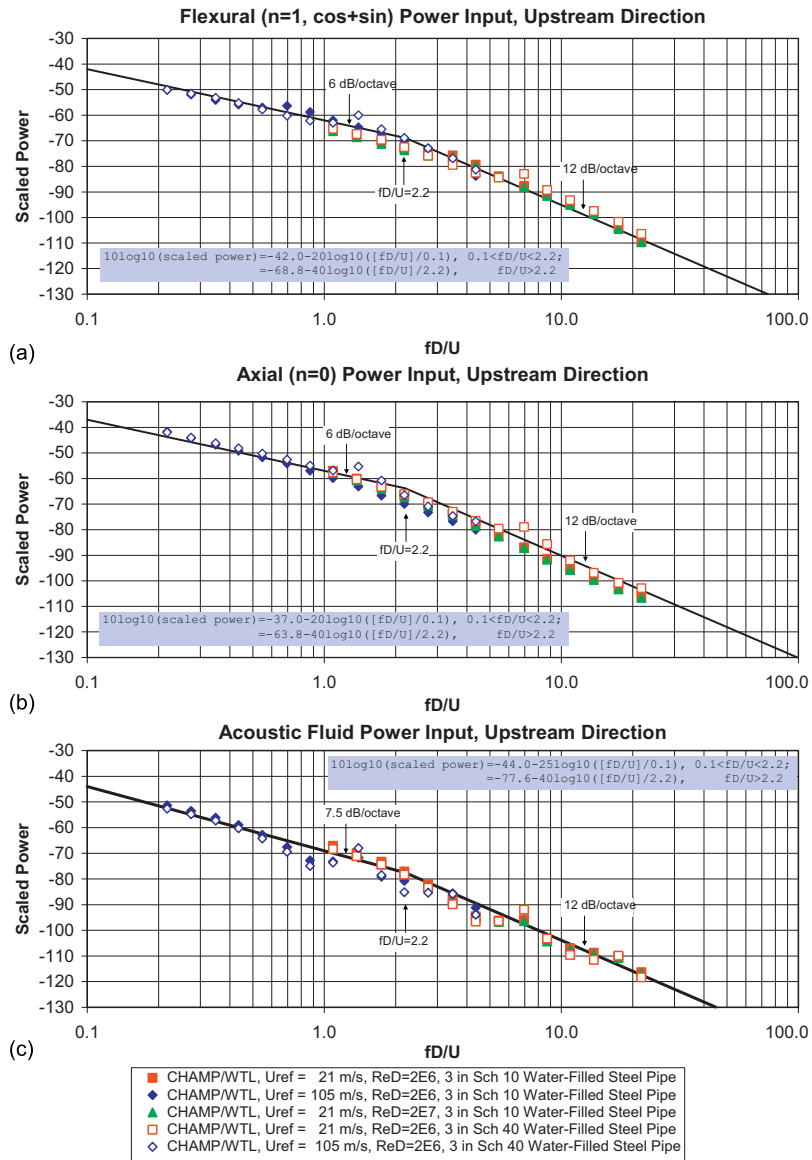


Fig. 17. Empirical curve fits of scaled, simulated power in (a) $n = 1$ flexural, (b) axial, and (c) acoustic waves emanating from TBL-excited water-filled 76.2 mm (3 in) steel elbows, in the upstream direction, as a function of flow speed, pipe schedule, and Reynolds number.

range between $0.22 < fD/U_o < 22$. The collapse of data is good, but not perfect (a perfect collapse using the simple scaling described here is unlikely for a complex structure like an elbowed pipe). The flexural and axial power data have different slopes over different frequency ranges, with a breakpoint at about $fD/U_o = 2.2$. The flexural and axial powers collapse better than the acoustic powers, where the acoustic power data has a discontinuity near $fD/U_o = 1$. Figs. 5 and 6 show that the slopes of the TBL wall pressure autospectra also change between fD/U_o of 1 and 5, causing the breakpoint in the slopes of the power spectra.

4.3. Empirical power input

The scaled power spectra may be used to infer empirical formulae for the spectral amplitudes of the power in each wavetype, in both the upstream and downstream directions. Since the data all seem to change in slope at fD/U_o of about

2.2, we form two-part functions:

$$\begin{aligned} P_{\text{scaled}}(\text{dB}) &\cong P_1 - m_1 10 \log_{10}([fD/U_o]/0.1), & 0.1 > fD/U_o < 2.2, \\ &\cong P_2 - m_2 10 \log_{10}([fD/U_o]/2.2), & fD/U_o > 2.2. \end{aligned} \quad (30)$$

To generate a power spectrum for any combination of flow and structural parameters, simply subtract $10 \log_{10} \left[\sum Z_{\text{wavetype}(s)} \alpha_3 \text{Re}_D^{1/7} / (\alpha_1^3 \rho_{\text{fluid}}^2 U_o^3 D_{\text{pipe}}^3 L_{\text{elbow}}^2) \right]$ from P_{scaled} , and compute a dimensional frequency f by multiplying fD/U_o by U_o/D .

Values for P_1 , P_2 , m_1 , and m_2 are listed for each wavetype and direction in Table 2, and examples of the curve fits for flexural ($n = 1$), axial ($n = 0$), and acoustic ($n = 0$) powers in the downstream direction are shown in Fig. 17. The curves are generally conservative, tending toward the upper data points. However, some of the data points are above the curves. If more conservative estimates of the power spectra are required, the curves may be shifted upward by a few dB. However, since the TBLFF wall pressure autospectra may be biased high at higher frequencies (see the discussion at the end of Section 3.2.1), the curves above fD/U_o of 2.2 are likely already conservative.

5. Summary and conclusions

We have described a procedure which couples CFD and structural–acoustic models that may be used to compute the structure- and fluid-borne powers emanating from the ends of TBL excited piping components. The procedure is illustrated for a 90° piping elbow with a radius to diameter ratio of 1.5. Based on wall pressure fluctuations computed from CFD RANS solutions, the TBL loading on the piping downstream of the elbow is high, so that an effective elbow noise source includes several diameters of piping downstream of the elbow. The pipe walls are represented with finite elements, and the internal fluid simulated with boundary elements. The fluid is coupled to the structural walls so that excitation of the walls generates acoustic waves in the fluid. Semi-infinite impedances for all structural wavetypes and acoustic waves based on WTL models are applied to the ends of the elbow, and power spectra in each wavetype are computed using the CHAMP capability.

Powers in wavetypes upstream and downstream of the elbow are computed for Schedules 10 and 40 76.2 mm (3 in) steel pipe filled with water at 21 and 105 m/s, and at Re_D of 2×10^6 and 2×10^7 . Since the power levels vary significantly for the different parameter combinations, scaling relationships are used to collapse the simulated data, and empirical curves are fit to the data. A set of empirical formulae are provided for the power spectra in all wavetypes, and may be used to compute power spectra for geometrically similar 90° piping elbows using other combinations of flow and structural parameters not considered here. The formulae, however, are based on the limited set of computations reported here. In the future, additional configurations may be considered and used to refine the empirical curves.

Now that the procedure for computing powers emanating from piping components excited by distributed random forces has been established, it may be used to estimate equivalent source strengths for any general shape excited by distributed internal sources. The power inputs may be applied to wave-based (WTL) and transfer matrix based pipe modeling approaches to estimate vibro-acoustic response elsewhere in a connected piping system, as well as to Statistical Energy Analysis (SEA) models.

Table 2
Summary of constants for empirical curve fits to scaled power spectra for TBL-excited 90° elbow.

Wavetype, direction	Power P_1 (dB), $fD/U = 0.1$	Slope m_1 , $fD/U < 2.2$	Power P_2 (dB), $fD/U = 2.2$	Slope m_2 , $fD/U > 2.2$
Fluid, upstream	−44	2.5	−77.6	4
Fluid, downstream	−42	2.5	−75.6	4
Axial $n = 0$, upstream	−37	2	−63.8	4
Axial $n = 0$, downstream	−40	2	−66.8	4
Torsion $n = 0$, upstream	−48	1.5	−68.1	3.5
Torsion $n = 0$, downstream	−42	2	−68.8	3.5
Flexural $n = 1$, upstream	−42	2	−68.8	4
Flexural $n = 1$, downstream	−40	2	−66.8	4
Flexural $n = 2$, upstream	−38	2	−64.8	4
Flexural $n = 2$, downstream	−35	2	−61.8	4

Several extensions to this work are possible. The results presented here are for a specific elbow radius to pipe diameter ratio. Tighter and more gradual elbows could be considered in the future. Since in practice many pipes are connected by large flanges, the scattering effects of the flanges could be considered. Including flange effects would likely require including convective terms in the fluctuating forces acting on the walls (the convective terms are ignored in this study since they are negligible). Also, the acoustic power induced by turbulence passing through mean velocity gradients in the core flow through the elbow could be computed. Finally, other geometries, like U-bends and T-junctions could be modeled.

Acknowledgements

This work was sponsored by the Office of Naval Research, Stephen Schreppler and William Martin, program managers. The authors also acknowledge the support of the Applied Physical Sciences Corporation (Ann Stokes and Charles Corrado) for providing WTL data to the authors. The authors also acknowledge helpful discussions with the technical staff of the ESI software group.

Appendix A. Estimating effective edge velocities and displacement thicknesses in complex pipe flow profiles

Most empirical estimates of TBL wall pressure fluctuations are based on ideal flat plate, straight channel and straight pipe flow measurements and therefore rely on quantities such as boundary layer displacement thickness and boundary layer edge velocity. Boundary layer displacement thickness is defined as the distance by which the solid boundary would have to be displaced in a frictionless flow to give the same mass flow rate deficit as exists in the boundary layer, so

$$\delta^* = \int_0^\infty \left(1 - \frac{u}{U}\right) dy \approx \int_0^\delta \left(1 - \frac{u}{U}\right) dy, \quad (\text{A.1})$$

where y is the distance normal to the wall, u the component of the velocity tangential to the wall, U the freestream velocity, and δ the disturbance thickness, usually defined as the distance from the surface to the point where the velocity is within 1% of the freestream velocity. For turbulent flow over a flat plate, it can be shown that $\delta^* = \delta/8$ (Burmeister, 1993). The edge velocity is defined as $U_{\text{edge}} = u(\delta)$.

These quantities are only well defined for flat plate (or at least external) flows, where there is a clearly defined edge separating the boundary layer from the freestream. Quantities that are generally used to characterize duct flows, such as hydraulic diameter and bulk velocity, are not sufficient to characterize spatial variations that occur along the length of the duct. Therefore, a characteristic length and velocity is needed that can be used to correlate wall pressure fluctuations with velocity profiles in arbitrary, three-dimensional and especially internal flow fields. We employ a blending function in a two-layer turbulence model to use in this respect.

Menter's blending function (1992, 1994), which is defined as

$$F_1 = \tanh(\text{arg}_1^4), \quad (\text{A.2})$$

is designed to equal 1.0 in the sublayer and log-layer and decrease to zero in the wake region of a shear layer. In Eq. (A.2),

$$\text{arg}_1 = \min \left[\max \left(\frac{\sqrt{\bar{k}}}{0.09\bar{\omega}y}, \frac{500v}{y^2\bar{\omega}} \right); \frac{4\rho\sigma_{\omega 2}\bar{k}}{CD_{\bar{k}\bar{\omega}}y^2} \right], \quad (\text{A.3})$$

where

$$CD_{\bar{k}\bar{\omega}} = \max \left(2\rho\sigma_{\omega 2} \frac{1}{\bar{\omega}} \frac{\partial \bar{k}}{\partial x_j} \frac{\partial \bar{\omega}}{\partial x_j}, 10^{-20} \right), \quad (\text{A.4})$$

where $\sigma_{\omega 2}$ is the diffusion coefficient in the \bar{k} - $\bar{\omega}$ -SST turbulence model. The term arg_1 (and thus F_1) goes to zero as $y \rightarrow \infty$, which is clear due to the $1/y$ or $1/y^2$ dependence of all three arguments in Equation (A.3). The first argument is equal to the turbulent length scale, $\ell = \sqrt{\bar{k}}/(0.09\bar{\omega}) = \bar{k}^{3/2}/\varepsilon$, divided by y . It is equal to 2.5 in the log-layer and goes to zero towards the boundary layer edge. The second argument ensures that F_1 is equal to one in the sublayer. Menter points out that $\bar{\omega}$ is proportional to $1/y^2$ in the near wall region and proportional to $1/y$ in the log region, so $1/(\bar{\omega}y^2)$ is constant near the surface and goes to zero in the log region. The third argument is “an additional safe guard against the “degenerate” solution of the original \bar{k} - $\bar{\omega}$ model with small freestream values for $\bar{\omega}$.”

A Reynolds-averaged Navier–Stokes solution using the Menter $\bar{k} - \bar{\omega}$ -SST model was obtained for turbulent flow over a flat plate at a Reynolds number (based on plate length) of $Re_L = 4 \times 10^7$ using a sublayer-resolved grid. Slug flow was assumed at the plate leading edge and far-field values of $\bar{k}_\infty = 1 \times 10^{-7} V_\infty^2$ and $\bar{\omega}_\infty = 9 V_\infty/L$ (such that $\mu_{T_\infty}/\mu = 0.45$) were assumed at the inlet and at $y/L = 0.125$. Profiles of the blending function, F_1 , were taken normal to the wall and used to find the location (y_{99}) where F_1 first drops from 1.0 down to 0.99, which occurs in the wake region of the boundary layer. Comparing this distance to the disturbance thickness of the boundary layer, it was found that $\delta \approx 1.8y_{99}$, so under the assumption of turbulent flow, $\delta^* \approx (1.8/8)y_{99}$. Similarly, it was found that $U_{edge} \approx 1.1U(y_{99})$.

Subsequently, a solution was obtained for turbulent flow through a 90° bend at Reynolds numbers (based on a pipe diameter of 0.082805 m) of 2×10^6 (water at 21 m/s). Profiles of velocity and F_1 were taken normal to the pipe wall. At each point, the distance y was measured from the surface to the point where $F_1 = 0.99$, and this value of y was used to determine δ^* and U_{edge} through the equations specified above.

Fig. 18 shows slices of the velocity magnitude extending downstream of the pipe bend. Fig. 19 shows a fully developed velocity profile upstream of the pipe bend. For this profile, F_1 maintains a nearly constant value of 1.0 across the diameter of the pipe except for a slight dip near $y=D/2$. Since F_1 never drops below the specified cut-off value of 0.99, y_{99} is specified as $y_{99} = 0.5D$ and U_{99} is specified as $U_{99} = 1.1 V_{ref}$. The yellow diamond in Fig. 19 marks this point. Then

$$\delta^* = 1.8(y_{99}/8) = 0.1125D = 0.00932 \text{ m, and } U_{edge} = 1.1 U_{99} = 1.21 V_{ref} = 25.41 \text{ m/s.}$$

Fig. 20 shows a velocity profile near the exit of the computational domain, taken from $\theta = 90^\circ$ to 270° (i.e., extending from bottom to top in Fig. 18). For this profile, F_1 drops off rapidly toward zero for both inner and outer boundary layers. The yellow diamonds in Fig. 20 mark y_{99} for both points. For the inner boundary layer (associated with $\theta = 90^\circ$), $y_{99} = 0.275D$, so

$$\delta^* = 1.8(y_{99}/8) = 0.0618D = 0.00512 \text{ m,}$$

and $U_{99} = 1.04 V_{ref}$, so

$$U_{edge} = 1.1 U_{99} = 1.15 V_{ref} = 24.1 \text{ m/s.}$$

For the outer boundary layer (associated with $\theta = 270^\circ$), $y_{99} = 0.0466D$, so

$$\delta^* = 1.8(y_{99}/8) = 0.0105D = 0.000869 \text{ m,}$$

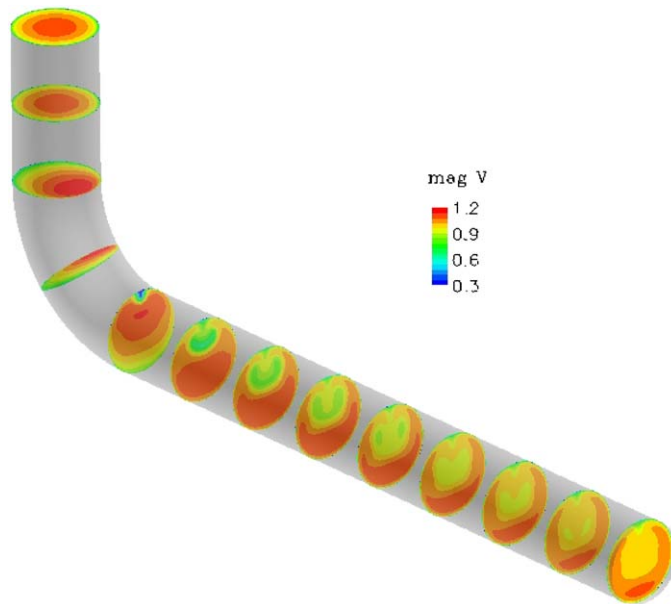


Fig. 18. Slices of velocity magnitude extending downstream of the pipe bend.

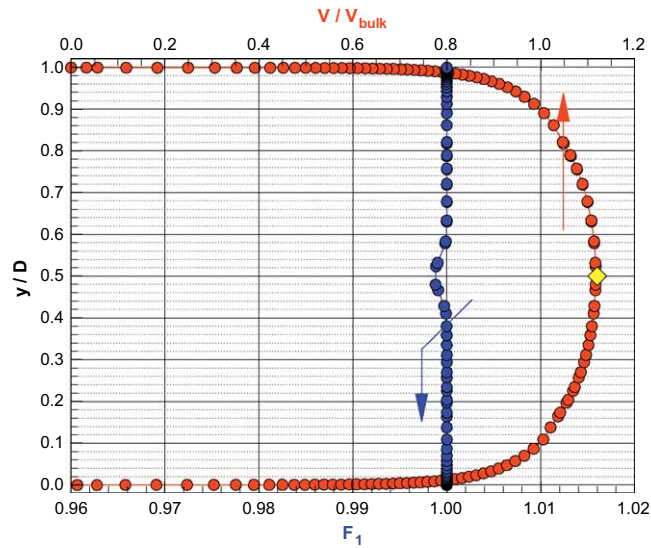


Fig. 19. Velocity profile and corresponding profile of F_1 in the fully developed region upstream of the pipe bend. Arrows denote the upper and lower axes corresponding to the profiles.

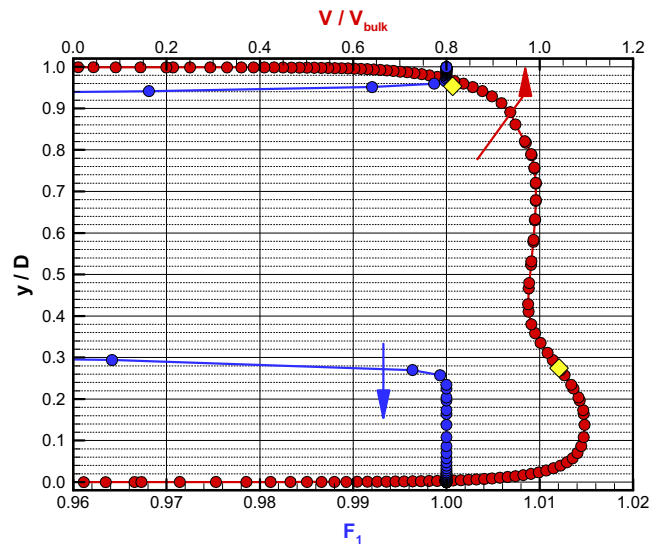


Fig. 20. Velocity profile and corresponding profile of F_1 near the exit of the computational domain downstream of the pipe bend. Arrows denote the upper and lower axes corresponding to the profiles.

and $U_{99} = 0.814 V_{\text{ref}}$, so

$$U_{\text{edge}} = 1.1 U_{99} = 0.895 V_{\text{ref}} = 18.8 \text{ m/s.}$$

References

- Anwer, M., So, R.M.C., 1993. Swirling turbulent flow through a curved pipe. *Experiments in Fluids* 14, 85–96.
 Au-Yang, M.K., Connelly, W.H., 1977. A computerized method for flow-induced random vibration analysis of nuclear reactor internals. *Nuclear Engineering and Design* 42, 257–263.

- Bendat, J.S., Piersol, A.G., 2000. In: *Random Data Analysis and Measurement Procedures* third ed. John Wiley and Sons.
- Blake, W.K., 1970. Turbulent boundary layer wall pressure fluctuations on smooth and rough walls. *Journal of Fluid Mechanics* 44, 637–660.
- Boersma, B.J., Nieuwstadt, F., 1996. Large-eddy simulation of turbulent flow in a curved pipe. *ASME Journal of Fluids and Engineering* 118, 248–254.
- Bull, M.K., 1967. Wall pressure fluctuations associated with subsonic turbulent boundary layer flow. *Journal of Fluid Mechanics* 28, 719–754.
- Burmeister, L.C., 1993. In: *Convective Heat Transfer* second ed. John Wiley and Sons.
- Conti, M., Corrado, C., and Stokes, A., 2001. Array based methods of characterizing piping component acoustic behavior. IMECE2001/NCA-23506. In: *Proceedings of the ASME 2001 IMECE*, New York, NY, USA, 11–16 November.
- Corcos, G.M., 1963. Resolution of pressure in turbulence. *Journal of the Acoustical Society of America* 35, 192–199.
- Davidson, L.C., Smith, J.E., 1969. Liquid–structure coupling in curved pipes. *Shock and Vibration* 40 (Part 4), 197–207.
- Davidson, L.C., Samsury, D.R., 1972. Liquid–structure coupling in curved pipes – II. *Shock and Vibration* 42 (Part 1), 123–136.
- Duong, P.T.H., 1980. A finite element method for the double-layer potential solutions of the Neumann exterior problem. *Mathematical Methods in the Applied Sciences*, 191–208.
- Enayet, M.M., Gibson, M.M., Taylor, A.M.K.P., Yianneskis, M., 1982. Laser Doppler measurements of laminar and turbulent flow in a pipe bend. *International Journal of Heat and Fluid Flow* 3, 213–219.
- Engbloom, J.J., Nelson, R.B., 1975. Consistent formulation of sound radiation from arbitrary structures. *Journal of Applied Mechanics Series E* 42, 295–300.
- Everstine, G.C., 1986. Dynamic analysis of fluid-filled piping systems using finite element techniques. *ASME Journal of Pressure Vessel Technology* 108, 57–61.
- Fahnlne, J.B., 2000. Fast acoustic power computations for structural optimization problems. *Journal of the Acoustical Society of America* 108, 2587.
- Fahnlne, J.B., 2009. Numerical difficulties with boundary element solutions of interior acoustic problems. *Journal of Sound and Vibration* 319, 1083–1096.
- Fahnlne, J.B., Koopmann, G.H., 1996. A lumped parameter model for the acoustic power output of a vibrating structure. *Journal of the Acoustical Society of America* 100, 3539–3547.
- Fahnlne, J.B., Koopmann, G.H., 1997. Numerical implementation of the lumped parameter model for the acoustic power output of a vibrating structure. *Journal of the Acoustical Society of America* 102, 179–192.
- Graham, W.R., 1997. A comparison of models for the wavenumber–frequency spectrum of turbulent boundary layer pressures. *Journal of Sound and Vibration* 206, 541–565.
- Hambric, S.A., Hwang, Y.F., Bonness, W.K., 2004. Vibrations of plates with clamped and free edges excited by low-speed turbulent boundary layer flow. *Journal of Fluids and Structures* 19, 93–110.
- Hambric, S.A., Hwang, Y.F., and Chyczewski, T.C., 2002. Noise sources and transmission in piping systems. IMECE2002/NCA-32682. In: *Proceedings of the ASME 2002 IMECE*, New Orleans, LA, USA, 17–22 November.
- Hambric, S.A., Jonson, M.L., Fahnlne, J.B., and Campbell, R.L., 2005. Simulating the vibro-acoustic power of fluid-loaded structures excited by randomly distributed fluctuating forces. In: *Proceedings of NOVEM 2005*, St. Raphael, France, 18–21 April.
- Hambric, S.A., Peltier, L.J., Fahnlne, J.B., Boger, D.A., and Poremba, J., 2003. Structural and acoustic noise sources due to turbulent flow through an elbow – formulation and analysis methods. IMECE2003/NCA-41525. In: *Proceedings of the ASME 2003 IMECE*, Washington, DC, USA, 16–21 November.
- Hayami, K., Brebbia, C.A., 1987. A new coordinate transformation method for singular and nearly singular integrals over general curved boundary elements. In: *In: Brebbia, C.A., Wendland, W.L., Kuhn, G. (Eds.), Boundary Elements, IX. Computational Mechanics Publications*, Southampton, pp. 379–399.
- Hayami, K., Matsumoto, H., 1994. A numerical quadrature for nearly singular boundary element integrals. *Engineering Analysis with Boundary Elements* 13, 143–154.
- Hwang, J.Y., Chang, S.C., 1991. A retracted boundary integral equation for exterior acoustic problems with unique solution for all wave numbers. *Journal of the Acoustical Society of America* 90, 1167–1180.
- Hwang, Y.F., 2002. Structural–acoustic wave transmission and reflection in a hose-pipe system. IMECE2002-32683. In: *Proceedings of the ASME 2002 IMECE*, New Orleans, LA, USA, 17–22 November.
- Hwang, Y.F., Bonness, W.K., and Hambric, S.A., 2003. On modeling structural excitations by low speed turbulent boundary layer flows. ARL/Penn State Technical Report 03-008.
- Hwang, Y.F., Bonness, W.K., Hambric, S.A., 2009. Comparison of semi-empirical models for turbulent boundary layer wall pressure spectra. *Journal of Sound and Vibration* 319, 199–217.
- Jacobs, L.D., Lagerquist, D.R., Gloyna, F.L., 1970. Response of complex structures to turbulent boundary layers. *Journal of Aircraft* 7, 210–219.
- Kawamura, T., Takahashi, M., 1996. Measurements of turbulent flow downstream from an elbow. In: *Chen, Shih, Lienau, Kung (Eds.), Flow Modeling and Turbulence Measurements*, vol. VI, pp. 175–182.
- Keith, W.L., Hurdis, D.A., Abraham, B.M., 1992. A comparison of turbulent boundary layer wall-pressure spectra. *ASME Journal of Fluids and Engineering* 114, 338–347.
- Ko, S.H., 1991. Analytical evaluation of a flush mounted hydrophone array response to a modified Corcos turbulent wall pressure spectrum. Naval Undersea System Center Technical Report TR 8943.

- Koopmann, G.H., Fahline, J.B., 1996. In: *Designing Quiet Structures*. Academic Press.
- Leissa, A., 1993. *Vibration of Shells*. Acoustical Society of America.
- Lesmez, M.W., Wiggert, D.C., Hatfield, F.J., 1990. Modal analysis of vibrations in liquid-filled piping systems. *ASME Journal of Fluids and Engineering* 112, 311–318.
- Manning, J.E., 2002. Statistical energy analysis of fluid-filled piping vibration and acoustics. IMECE2002-32685. In: *Proceedings of the ASME 2002 IMECE*, New Orleans, LA, USA, 17–22 November.
- Martinez, R., 1990. The thin-shape breakdown (TSB) of the Helmholtz integral equation. *Journal of the Acoustical Society of America* 90, 2728–2738.
- Menter, F.R., 1992. Improved two-equation $k-\omega$ turbulence models for aerodynamic flows. NASA TM 103975.
- Menter, F.R., 1994. Two-equation eddy viscosity turbulence models for engineering applications. *AIAA Journal* 32, 1598–1605.
- Peltier, L.J., Hambric, S.A., 2007. Estimating turbulent boundary layer wall pressure spectra from CFD RANS solutions. *Journal of Fluids and Structures* 23, 920–937.
- Powell, A., 1958. On the fatigue failure of structures due to vibrations excited by random pressure fields. *Journal of the Acoustical Society of America* 30, 1130–1135.
- Sgard, F., Atalla, N., Nicholas, J., 1994. Coupled FEM–BEM approach for mean flow effects on vibro-acoustic behavior of planar structures. *AIAA Journal* 32, 2351–2358.
- Stokes, A., Conti, M., Corrado, C., and Arzoumanian, S., 2001. A transmission line approach to the acoustic analysis of piping systems. IMECE2001/NCA-23507. In: *Proceedings of the ASME 2001 IMECE*, New York, NY, USA, 11–16 November.
- Strawderman, W.A., 1969. Turbulence-induced plate vibrations: an evaluation of finite- and infinite plate models. *Journal of the Acoustical Society of America* 46, 1294–1307.
- Wiggert, D.C., Tijsseling, A.S., 2001. Fluid transients and fluid–structure interaction in flexible liquid-filled piping. *Applied Mechanics Reviews* 54, 455–481.
- Wilby, J.F., 1967. The response of simple panels to turbulent boundary layer excitation. Technical Report AFFDL-TR-67-70.
- Wu, T.W., 1995. A direct boundary element method for acoustic radiation and scattering from mixed regular and thin bodies. *Journal of the Acoustical Society of America* 97, 84–91.